Department for Physics and Astronomy
University of Heidelberg

Master Thesis in Physics
submitted by

Lukas Endres

born in Bamberg (Germany)

2020

Cryogenic Characterization
of a Microchannel Plate Detector

This Master Thesis was carried out by Lukas Endres
at the
Max Planck Institute for Nuclear Physics in Heidelberg
under the supervision of
Priv.-Doz. Dr. Robert Moshammer
and
Prof. Dr. Thomas Pfeifer

A **cryogenic test setup for microchannel plate detectors** was built up and put into operation. Microchannel plates with a quality diameter of 120 mm and an open area ratio of 0.6 are tested. During measurements they can be cooled down to 35 K. A possibility to counteract the consequences of thermal contraction of different construction parts with CuBe cup springs was found. The thermal connection between the second stage of a coldhead and the channel plates was optimized using a copper braid and a suitable wiring of the detector. The final **saturation and linearity measurements** show that the used channel plates are nearly unaffected by a temperature change from room temperature to 35 K. Only the supply voltage where the channel plates operate near the saturation region is assumed to decrease slightly. The setup has to be further refined to enable a lower temperature for channel plate tests.

Ein **kryogener Teststand für Microchannel-Plate-Detektoren** wurde aufgebaut und in Betrieb genommen. Microchannel-Plates mit einem effektiven Durchmesser von 120 mm und einem Open Area Ratio von 0.6 werden getestet. Während der Messungen können diese bis zu einer Temperatur von 35 K gekühlt werden. Es wurde eine Möglichkeit gefunden den Konsequenzen der thermischen Kontraktion verschiedener Konstruktionselemente mit CuBe Tellerfedern entgegenzuwirken. Die thermische Ankopplung zwischen der zweiten Stufe eines Kaltkopfes und den Channel-Plates wurde optimiert, indem eine Kupfer-Litze hinzugefügt und eine geeignete Verkabelung gefunden wurde. Die finalen **Sättigungs- und Linearitätsmessungen** ergaben, dass die Channel-Plates bei einer Temperaturänderung von Raumtemperatur zu 35 K nahezu unbeeinflusst bleiben. Lediglich die Versorgungsspannung, bei der die Channel-Plates nahe der Sättigung betrieben werden, sank geringfügig. Der Aufbau muss dahingehend weiterentwickelt werden, dass die Channel-Plates bei niedrigeren Temperaturen getestet werden können.

Table of Contents

1. Motivation

My goal is simple. It is a complete understanding of the universe, why it is as it is and why it exists at all.

Hawking [1]

Occurrences in this domain are beyond the reach of exact prediction because of the variety of factors in operation, not because of any lack of order in nature.[a] Einstein [2]

---

[a]Although Einstein referred to the complexity of weather predictions, the statement can be transferred to a multitude of experimental measurements.

Stephen Hawking and Albert Einstein, two of the most famous thinkers of late modern times, comitted their lifes to physical insights. After the discovery of general relativity by Einstein in the early 20th century, Hawking focused on the theory of black holes and cosmological coherences. The problem with such theories is that they are typically far beyond the scope of surrounding conditions present on earth, so they can not be easily tested. Here the work of experimental physicists becomes important. Space observing imaging systems provided the first proofs for general relativity as the effect of gravitational lensing was discovered and for the existence of black holes by "simply" photographing one [3]. Spectroscopic methods taught us about the composition of stars and the interstellar medium. Thus, another interesting observation was made in the early 20th century. Eddington reported on the origin of "interstellar chemistry" after the discovery of spectral absorption lines in the spectrum of a star caused by the interstellar medium [4]. Nowadays, it is known that the absorption takes place in interstellar clouds, huge regions of cold matter of low densities in interstellar space. More recent spectroscopic experiments show that diffuse clouds are mainly monoatomic, while dense clouds also contain large and particularly stable molecules; around 50% of them being unusual at terrestrial standards [5]. Due to the lack of thermal energy, chemical reactions forming these

molecules are mainly triggered by collisions of the reactants themselves or of reactants with cosmic rays. Theory provides rate coefficients for a multitude of reactions but experimental confirmations are needed. Therefore (and for other experiments using cold molecular ions), the Cryogenic Storage Ring (CSR) was built at the Max Planck Institute for Nuclear Physics in Heidelberg - first announced in Zajfman et al. [6]. A concept and its technical realization were presented by von Hahn et al. [7]. The CSR is capable of creating a few Kelvin environment with residual gas pressures of down to a few 10^{-15} mbar, comparable to the interstellar medium. Injected atomic or molecular ions are electrostatically guided onto a closed trajectory. After the collision of the cold molecular ion beam with a supersonic gas jet a kinematically complete analysis of the produced fragments will be executed using a Reaction Microscope [8; 9; 10]. For particle detection microchannel plate detectors are used, the core of this work.

Due to the extreme environment inside the CSR, it has to be elaborated if the microchannel plate detector can provide sufficient detection efficiency. Especially for experiments where several fragments have to be detected coincidently a high detection efficiency is needed. The lower the efficiency, the longer acquiring significant statistics takes and the more expensive the measurement becomes. Contrary to that, heating the detector for higher efficiency should not have a significant effect on the costly produced measurement environment inside the reaction microscope. It is already known, that in general the efficiency decreases with temperature but for exact predictions the specific microchannel plate in use has to be characterized adequately. The main goal of this work is to characterize the behavior of the used channel plate detector in a cryogenic environment. A cryogenic test setup is built up and put into operation such that the detector can be tested at temperatures between 35 K and room temperature. The result of this work will contribute to the huge project CSR and its successful measurements which will conduce to new insights in the field of astrochemistry.

2. Relevant Considerations of Condensed Matter Physics

In this chapter a compact overview of the topics electrical conductivity and thermal contraction is given. Since general properties of solids is a wide ranged field we only focus on the aspects relevant for this thesis. More information is given in typical condensed matter literature i.e. Hunklinger [11], Chapter 3-10, and Gross Marx [12], Chapter 1,2 and 4-10. The main goal is to achieve insights into the temperature dependent electrical properties of amorphous semiconductors i.e. glasses, out of which Micro-Channel Plates (MCPs) are made.

2.1. Electrical Conductivity

A large class of solids can be treated as a periodic structure where the smallest repeating unit is called primitive cell. Those primitive cells are essential for the properties of a solid, because they define the Brillouin zones which contain all possible momentum vectors $\vec{k}$ describing lattice oscillations in real space (= phonons). Since phonons play a bigger role in the transport of thermal energy, the focus in the following analysis will be layed on the energy band model for electrons inside a periodic potential. Similar to the phonons, electrons can be fully described by restriction to the first Brillouin zone. The potential landscape then reduces to the energy band structure, see Hunklinger [11], Chapter 8.5 and Gross Marx [12], Chapter 8.

2.1.1. Electrical Transport in Metals

If one wants to understand the processes relevant for the transport of electrical charge inside a solid, one has to understand the interactions of

conducting electrons with the solid itself. The clearest model is developed for metals which have a full valence band and a partially filled conduction band. The first proper model describing electrical conduction in metals was presented by Drude. He used the classical picture of a free electron gas which is a good assumption for electrons in the conduction band of metals, with average drift velocity v_d and relaxation time τ. Although he neglected the Fermi-Dirac distribution and hence followed a wrong calculation, he ended up with the correct solution for the electron mobility μ and the conductivity σ:

$$\mu = \frac{e\tau}{m_e}, \tag{2.1}$$

$$\sigma = \frac{ne^2\tau}{m_e} = ne\mu, \tag{2.2}$$

with the electron mass m_e, the electron density n and the elementary charge e.
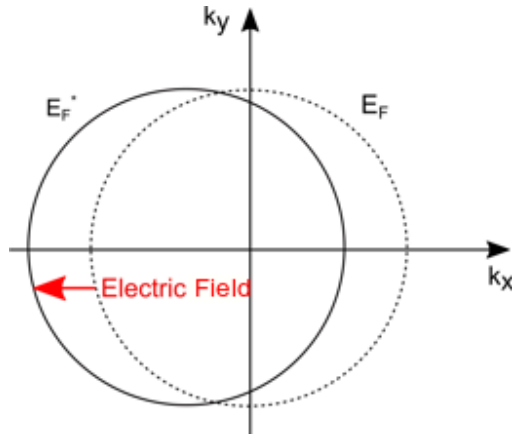
Figure 2.1.: Scheme of the displacement of the Fermi energy surface in momentum space. The initial Fermi sphere E_F is displaced by a constant electric field until the equilibrium state E_F^* is reached. In this scheme the applied electric field is oriented parallel to the spatial x-axis, hence the Fermi sphere moves in x-direction.

A more advanced approach was later presented by Sommerfeld. He treated the electrons as quasi-free fermions, following the Schrödinger equation and

the Pauli principle. The model itself uses the Fermi surface of electrons and its interaction with an external constant electrical field $\vec{E}$. The E-field $\vec{E} = E\vec{e}$ pushes the Fermi surface in k-space $E_{\mathrm{F}}(\vec{k})$ in $\vec{e}$-direction, until a dynamic equilibrium is reached where scattering processes between electrons and e.g. phonons prohibit a further displacement of $E_F(\vec{k})$ (see Figure 2.1). Using the Boltzmann equation and the relaxation approach Sommerfeld calculated for the conductivity σ of an isotropic gas of free electrons

$$\sigma = \frac{e^2}{3\pi^2} \frac{\tau(E_{\mathrm{F}})}{m^*} k_F^3 = \frac{ne^2}{m^*}\tau(E_F), \tag{2.3}$$

with the effective electron mass m^*, the electron density n and the wave vector $k_{\mathrm{F}} = \sqrt[3]{3\pi^2 n}$ of those electrons with Fermi Energy E_{F}. To reach this result he also assumed that only electrons near the Fermi energy contribute to the electrical charge transport. The essential part of Equation 2.3 is the relaxation time τ which determines the time until the Fermi surface reaches equilibrium after turning on the electrical field. τ is the result of different scattering processes and therefore characteristic for different temperature regions:

i) electron-electron scattering: (τ_{e}),

ii) electron-phonon scattering: (τ_{p}),

iii) electron-defect scattering: (τ_{d}).

Since (i-iii) are independent scattering processes one can write

$$\frac{1}{\tau} = \frac{1}{\tau_{\mathrm{e}}} + \frac{1}{\tau_{\mathrm{p}}} + \frac{1}{\tau_{\mathrm{d}}}. \tag{2.4}$$

For very clean metals with high purity and few vacancies mainly electron-phonon scattering is present. At high temperatures $(T > \theta)$[1] the electrons mainly scatter with phonons at Debye frequency. According to the inverse mean free path $l^{-1} = n_{\mathrm{ph}} \cdot \sigma_{\mathrm{scat}}$, using a constant cross section σ_{scat} for electrons near E_{F} and phonons of frequency ω_{Debye}, the temperature dependency in this region is characterized by the phonon density n_{ph}. At high

---

[1]θ is the so called Debye temperature, a material dependent constant. It is linked to the maximum frequency of phonos ω_{Debye} present in a solid.

temperatures T, it applies $n_{\mathrm{ph}} \propto T$ which yields to $l^{-1} \propto T$ and finally gives $\sigma \propto l \propto T^{-1}$.

With decreasing temperature the total number of phonons and their frequency decreases. Here one has to apply the Bloch-Grüneisen law for the resistivity $\rho \propto \sigma^{-1}$ which is valid for all metals where electron phonon scattering is dominant:

$$\rho = A \left(\frac{T}{\theta}\right)^5 \int_0^{\theta/T} \frac{x^5 \mathrm{d}x}{(e^x - 1)(1 - e^{-x})}. \tag{2.5}$$

Without going into detail one calculates:

$$T \to 0 : \ \rho \propto \left(\frac{T}{\theta}\right)^5, \tag{2.6}$$

$$T \to \theta : \ \rho \propto \left(\frac{T}{\theta}\right). \tag{2.7}$$

At temperatures near absolute zero ($T < 10\,\mathrm{K}$) phonons are negligible and a constant number of lattice defects are left as scattering partners. In total the temperature dependent resistivity of metals can be described as following:

$$\rho \propto \begin{cases} const & : \ T \ll \theta \ \text{(only defects)}, \\ T^5 & : \ T < \theta, \\ T & : \ T > \theta. \end{cases} \tag{2.8}$$

The resistance of metals decreases with temperature until a constant value which depends on the number of defects in the metal, is reached.

2.1.2. Electrical Transport in Semiconductors

The main difference between metals and semiconductors is the number of occupied states in the conduction band. While the conduction band in metals is occupied by electrons independently of temperature, the conduction band of semiconductors gets populated by thermally excited electrons which are lifted from the valence band. The essential quantity is the band-gap

energy $E_g = E_c - E_v$, with the minimum energy of the conduction band E_c and the maximum energy of the valence band E_v. The band gap is typically in the order of a few eV, for example silicon has a band gap of $E_g = 1.1\,\text{eV}$. Hence, a semiconductor behaves as an insulator at $T = 0\,\text{K}$. This implies a zero-crossing of the mobility at absolute zero. With increasing temperature electrons start to occupy the conduction band and the semiconductor becomes electrically conductive.

One distinguishes between intrinsic and doped semiconductors. The former ones have in common that the number of electrons in the conduction band is always equal to the number of holes in the valence band. The latter ones contain foreign atoms which dramatically influence the electrical properties by delivering free electrons to the conduction band (donators) or by extracting electrons out of the valence band (acceptors).
As shown in Section (2.1.1) the mobility of electrons and hence the electrical conductivity of solids is mainly restricted by scattering processes. Again the dominant process in a definite temperature region determines the temperature dependent electrical conductivity. For small temperatures ($T \approx 50\,\text{K}$) electron-impurity scattering is dominant while for higher temperatures electron-phonon scattering is dominant. One finds:

$$\mu \propto \begin{cases} T^{3/2} & : \ T < 50\,\text{K}, \\ T^{-3/2} & : \ T > 50\,\text{K}. \end{cases} \tag{2.9}$$

2.1.3. Electrical Transport in Amorphous Solids

In amorphous semiconductors one has to modify the relaxation and scattering approach, since the periodic structure used to analyze metals or regular semiconductors is missing. The band structure of a crystal is formed by the periodicity of atomic levels, this is restricted to a near field ordering in amorphous solids. N.F. Mott described this fact with localized and delocalized states (see Figure 2.2) and hence paved the way for the description of electrical conductivity in amorphous solids. Due to the high level of disordering, electrons cannot be described as Bloch waves which globally leads to a highly suppressed mobility. Also, the Fermi energy temperature independently coincides with the maximum of the defect levels (see Figure 2.2).
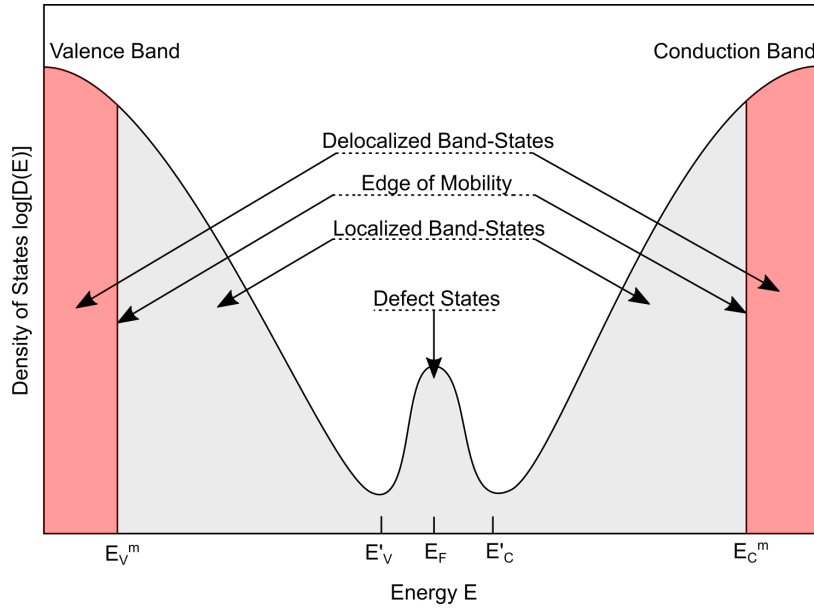
Figure 2.2.: The model of localized and delocalized states is schematically presented where the schematic idea is taken from [11]. One sees the differentiation between regions of localized (grey shaded) and delocalized (red shaded) states in the band structure of amorphous semiconductors. The maximum of defect states lies in the middle of a local band gap and coincides with the Fermi energy. The indicated energy levels are further described in the text.

One describes three temperature regions: high temperatures, room temperature and low temperatures. In the first region the transport of electrical charge takes place in the delocalized levels. The conductivity can be described by:

$$\sigma = \sigma_0 e^{-(E_{\mathrm{C}}^{\mathrm{m}} - E_{\mathrm{F}})/k_{\mathrm{B}}T}, \tag{2.10}$$

with some experimental constant σ_0, the Boltzmann constant k_{B} and the energy at the mobility edge of the conduction band $E_{\mathrm{C}}^{\mathrm{m}}$ (see Figure 2.2).

At room temperature the localized levels are occupied and Hopping becomes the dominant process for electron transport (see Figure 2.3).
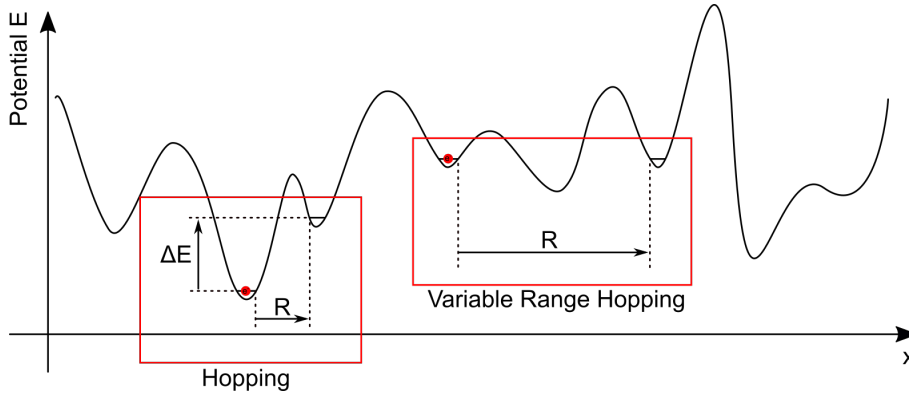
Figure 2.3.: Depiction of Hopping and Variable Range Hopping in one dimension. One sees two exemplary electrons positioned in two minima along the potential landscape of an amorphous solid. Hopping is divided into absorption of thermal energy ΔE and tunneling (rate R) to an adjacent minimum. For Variable Range Hopping a minimum at an energy similar to the initial energy is needed. At the expense of tunneling rate R the electron tunnels into a level located at higher distance.

Electrons absorb thermal energy and tunnel into a neighboring localized level. The Hopping-rate reads:

$$\nu = \nu_0 \underbrace{e^{-\Delta E/k_B T}}_{\substack{\text{thermal}\\\text{excitation}}} \underbrace{e^{-2R/\alpha}}_{\substack{\text{tunneling}\\\text{probability}}} , \tag{2.11}$$

with the oscillation frequency ν_0 of the electron inside the potential, the tunneling rate R and the length of localization α.

For low temperatures the electrons occupy levels near the defect level and hence near the Fermi energy. The electrons have less thermal energy available for hopping into near-by states, so the process varies towards "Variable Range Hopping". At the expense of tunneling probability, due to less overlap with the wavefunction of energetically available target levels, they jump into a spatially more distant potential minimum (see Figure 2.3). For this to happen, they need a level with sufficiently small energy difference ΔE in a volume $\frac{4}{3}\pi r^3$ with radius r. The number of these states is $\frac{4}{3}\pi r^3 \cdot D(E_F) \cdot \Delta E$, with the density of states near the Fermi energy

$D(E_F)$. For the most probable jumps in a three-dimensional sample with $E_F =$ constant one calculates:

$$\sigma = \sigma_0 \exp\left[-\left(\frac{T_0}{T} \right)^{n=1/4} \right], \tag{2.12}$$

with the constant $T_0 \approx \frac{2.06^4}{\alpha^3 D(E_F) k_B}$. For two-dimensional samples one receives an exponential dependency of $n = 1/3$.

2.1.4. Electrical Transport in MCPs

Lead glasses, as well as doped silicate glasses, out of which MCPs are produced, belong in general to the class of amorphous semiconductors. Roth and Fraser [13] reported data which can be split into two temperature regions (see Figure 2.4). They discussed the models of Variable Range Hopping for two-dimensional surface structures and tunneling conduction[2] but these models could not explain the measured data completely. The difficulty in modeling the conductive behavior of MCPs in the cryo-region is a mixture of the decrease of available conduction electrons due to the lack of thermal energy and the possibly very complex atomic structure (near- and far-order) of amorphous materials. An important result of the data (Figure 2.4) is the increase of specific resistivity of approximately six orders of magnitude when cooling from room-temperature to $20\,\mathrm{K}$.

2.2. Linear Thermal Contraction

Commonly, one introduces phonons by calculating the next-neighbor interaction of atoms in a linear chain. While doing so, the bonding energy is approximated by a harmonic potential. Only near the minimum of the bonding energy this approach is reasonable, i.e. for small phonon energies (oscillations with low frequencies). With increasing temperature the mean phonon energy grows and hence the inharmonicity increases (see Figure 2.5). In a harmonic potential the mean distance between interacting partners stays constant with temperature, whereas the inharmonicity of the system

---

[2]Also, Smith [14] used a two-component model to describe the resistance characteristics of MCPs.
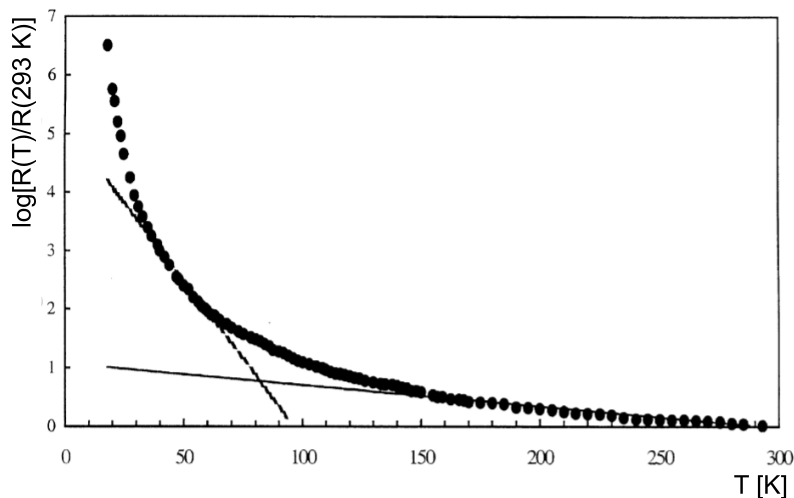
Figure 2.4.: Temperature dependent resistance data for a MCP with room-temperature resistance $R \approx 4.6\,\text{M}\Omega$, shown in Roth and Fraser [13]. The data gives rise to the determination of two temperature regions, in which a fit was executed (straight asymptotes). The resistance increases by six orders of magnitude when cooling from 293 K to 20 K.

causes a deviation from the mean distance. Transferred to the bonding energy in solids, length and volume increases with temperature. In the linear approximation the change of length is given by:

$$\Delta L = \alpha_L L_0 (T_2 - T_1), \tag{2.13}$$

with the thermal expansion coefficient α_L, the length L_0 at temperature T_1 and the final temperature T_2. α is a material dependent constant, describing the change of atomic equilibrium distances when changing the temperature. Typical values are in the order of $10^{-5}\,\text{K}^{-1}$.
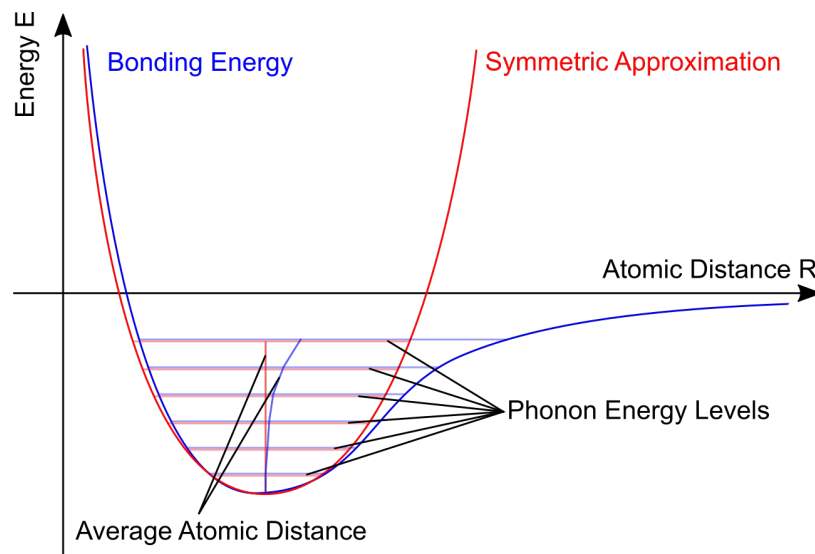
Figure 2.5.: Schematic explanation for thermal expansion. The bonding energy between two interacting atoms (blue) is approximated by a harmonic potential (red). For each curve the phonon energy levels are shown. While for the harmonic approximation the mean distance between the atoms stays constant, the real energy curve leads to an increased average atomic distance for increasing phonon energy.

3. Microchannel Plate Detectors

A Micro-Channel Plate (MCP) is an array of many microscopic electron multiplier tubes (channels) with length L and diameter d oriented parallel inside a lead glass. The length-to-diameter ratio $\alpha = L/d$ is an important quantity characterizing the channel plate performance. Typical values are $\alpha = 40\text{-}60$ with a channel length of a few millimeters. The channels reach from the front to the back end of the MCP where both sides are electrically contacted via a metallic coating. The advantage of MCPs used in particle detectors is a high efficiency for event detection with the ability of detecting single particle events and resolving them in time and space [15]. Although their technical properties and working principles are well understood for more than 50 years, there is still ongoing research concerning MCP development and usage. For example, in 2019, an US patent was published presenting a 3D-printing technique for MCP production [16].

The following sections will give an introduction about working principles of MCPs and the basic parameters describing MCPs. It will be discussed how to operate an MCP and how to acquire position resolved data.

3.1. Basic Parameters of MCPs

The channels of MCPs work as independent electron multiplier tubes [17]. An incident particle colliding with the channel wall produces δ secondary electrons. By applying an external electric field one accelerates these electrons towards the back end of the channel. Further collisions take place and each accelerated electron produces further δ secondary electrons. This reaction cascade is repeated n times until a total of δ^n electrons are emitted from the end of the channel (see Figure 3.1). A theoretical, probabilistic description of secondary electron emission in general can be found in [18], whereas [17] presents a Monte-Carlo-based model referring on the operation

of an MCP. In principle electrons, as well as ions or energetic photons, can produce secondary electron emission (SEM) with different efficiencies [19].
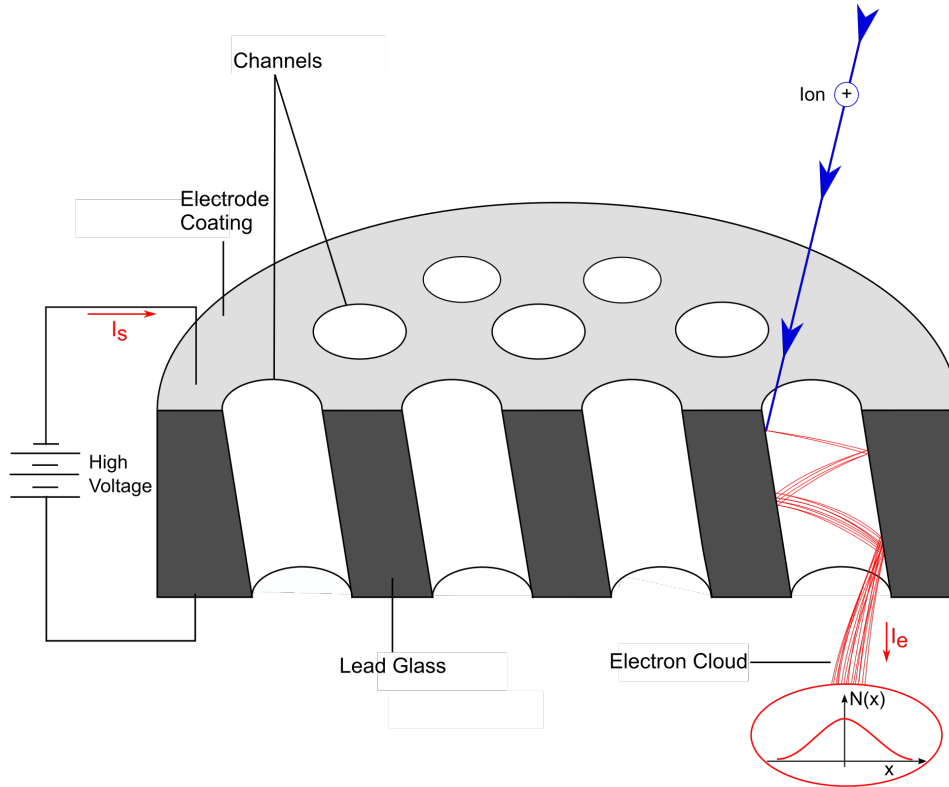

Figure 3.1.: Schematic depiction of an MCP. A high voltage source is connected to the metallic coating at the front and back end of the MCP. An incident positively charged ion triggers the SEM reaction cascade, producing the emission of an electron cloud at the end of a single channel and leads to an output current I_e. The electron cloud satisfies the one-dimensional (in general two-dimensional) spatial distribution $N(x)$, as indicated on the lower right. The electron replacement inside the channel wall material is provided by the external voltage source with a so called "strip current" I_s.

3.1.1. Saturation Properties

The total number of emitted electrons determines the gain G i.e. the amplification factor of an incident particle. As the secondary electron yield is a function of incident energy [20], the total gain is dependent on the applied voltage U_s. The more the secondary electrons are accelerated inside the channel, the higher is the secondary electron yield for each individual collision. Nevertheless, the gain can not grow to infinity; there are restrictions like space charge saturation, ion feedback and heating of the MCP due to a higher strip current:

  i) As mentioned in Section 2.1.4 the electrical conductivity of the MCP material increases with temperature. An increasing strip current due to a higher supply voltage causes a temperature increase inside the MCP material, further lowers the resistance and therefore increases the strip current, while the supply voltage stays constant. Hence applying a too large supply voltage may result in breaking the channel plate. Dark spots, due to melted MCP-areas may appear in position resolved measurements.

 ii) Space charge saturation is caused by Coulomb repulsion of emitted electrons. When the electron density at the channel output is too high, electrons repel each other causing a broadening of their spatial distribution and a lower spatial resolution.

iii) Ion feedback is triggered in the high electron density region at the channel end. High energy electrons collide with residual gas atoms or atoms which were desorbed from the channel wall and produce a positively charged ion. Following the voltage gradient the ions travel back to the channel front side and result in another SEM cascade distorting the original signal.

Typical numbers for unsaturated operation of channel plates are $G = 10^6$, $U_\mathrm{s} = 2.5\,\mathrm{kV}$ and a channel diameter of 10-20 µm micrometers.

   Overheating due to high strip current (i) can be prevented easily by applying proper supply voltages. Dependent on the chosen channel plate and its room-temperature resistance a few kilovolts are in general sufficient.

Space charge saturation (ii) is proportional to the channel diameter [21; 22]. A channel with diameter $d = 10\,\mu m$ saturates at gains of about 10^6. One possibility to exceed this value would be a larger channel diameter but this would result in a lower spatial resolution of emitted electrons and is strongly undesired for position-resolved measurements.
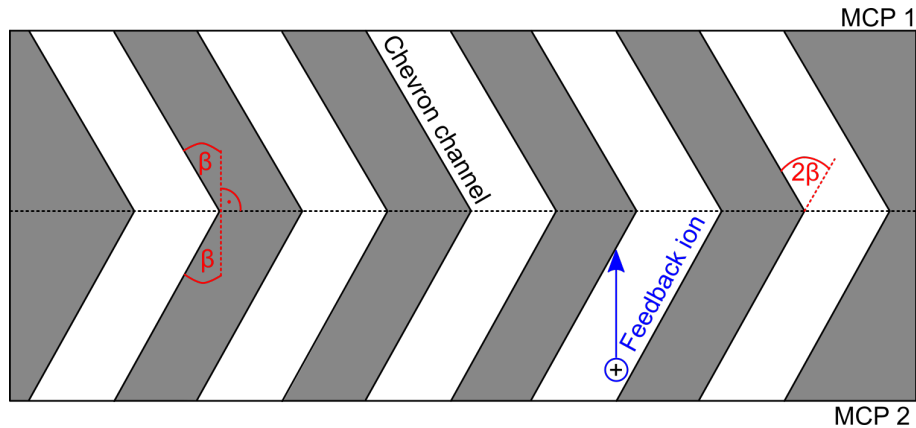

Figure 3.2.: Doubly stacked Chevron configuration of two MCPs. The two MCPs have identical bias angles β which are orientated in opposite direction. A feedback ion, produced at the channel end, is prohibited to travel to the front end of MCP 1.

The effect of ion feedback (iii) is lowered with the so called "Chevron" configuration (see Figure 3.2), first announced in Colson et al. [23]. One defines the bias angle β, included by the channel axis and the input surface normal. A Chevron configuration is built by stacking two MCPs with typically $\beta = 8°$ such that the channel axes point in opposite directions. The result of this procedure are "curved" channels (see Figure 3.2). Ions produced at the end of a channel are prevented to travel back to the channel front side. Instead the majority of feedback ions collides with the channel wall after shorter distances. Hence, less feedback noise is produced because reaction cascades caused by feedback ions are accelerated over a shorter distance. Operating both channel plates at individual gains of 10^4 and with a distance of $50\,\mu m$ yields a total (unsaturated) gain in the order of 10^7 [24]. By choosing higher supply voltages one can further increase these values

without exceeding the saturation limit.

3.1.2. Pulse Height Distribution

A common tool to evaluate the saturation status of an MCP is the Pulse Height Distribution (PHD). During experiments the time-resolved signal of the supply voltage is measured. Each SEM cascade produces a dip in the traced voltage signal. The amplitude of the dips is proportional to the number of electrons emitted by the channel end and hence proportional to the MCP gain. These pulse-shaped dips are used for position resolved measurements (as seen later, Section 3.3). Counting the amplitudes of each measured dip the PHD shows the number of counts related to amplitudes (see Figure 3.3). The PHD of unsaturated MCP operation is dropping exponentially, thus the real signal can not be distinguished from the underground. The PHD of saturated MCP operation shows a symmetric distribution after cutting off the underground. Since the signals' underground can be excluded most clearly when the MCP is working near the saturation limit, symmetric PHDs are used for MCP characterization when changing measurement parameters.

3.1.3. Efficiency and Dead Time

There are different factors determining the MCP's efficiency to detect an incident particle. An intuitive quantity is the Open Area Ratio (OAR), the ratio between active and total area of an MCP:

$$\text{OAR} = \frac{\text{Number of channels} \cdot \pi(d/2)^2}{A_{\text{MCP}}}, \tag{3.1}$$

with the channel diameter d and the total MCP area A_{MCP}. Besides the incident angle [25] the efficiency also depends on the species of incident particles. For example, Tatry et al. [26] reported a detection efficiency of about 80% for low energy protons and alpha particles using a single electron multiplier tube.

Each SEM reaction cascade depletes charge from the channel wall. Before a new event can be measured the channel wall has to be recharged with elec-
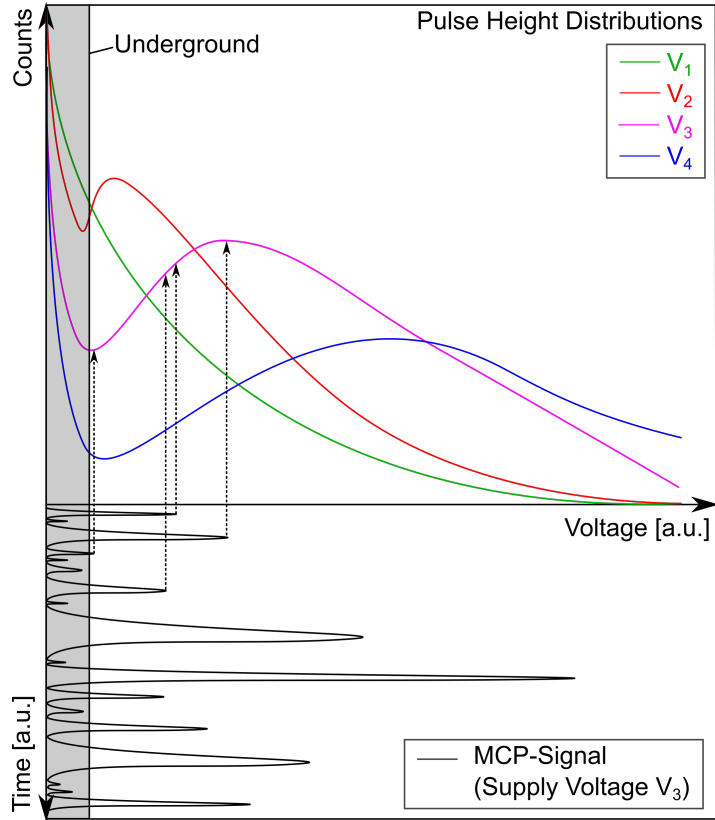
Figure 3.3.: Scheme of MCP-PHDs for different supply voltages V_i where $V_1 < V_2 < V_3 < V_4$. The green curve for V_1 shows an exponentially dropping PHD for unsaturated MCP operation. With increasing supply voltage a maximum is building up until a nearly symmetric PHD is reached at V_4 (blue curve). The MCP then operates near the saturation limit. In practice one wants to adjust the supply voltage such that a symmetric PHD is achieved.

trons. Assuming an exponential recharging process [27], the characteristic time constant τ reads:

$$\tau = k R_{\text{Ch}} C_{\text{Ch}} = k R_{\text{MCP}} C_{\text{MCP}}, \qquad (3.2)$$

with total MCP resistance R_{MCP} and capacitance C_{MCP}, the respective values for individual channels R_{Ch} and C_{Ch} and a constant k characterizing

an unspecified recharge circuit. Wiza [24] calculated for an MCP containing $5.5 \cdot 10^5$ channels with $R_{\mathrm{Ch}} = 2.75 \cdot 10^{14}\,\Omega$ the dead time τ as follows:

$$C_{\mathrm{MCP}} \approx 200\,\mathrm{pF} \Rightarrow C_{\mathrm{Ch}} \approx 3.7 \cdot 10^{-16}\,\mathrm{F}, \tag{3.3}$$

$$\Rightarrow C_{\mathrm{Ch}}^{\mathrm{eff}} \approx 7.4 \cdot 10^{-17}\,\mathrm{F}, \tag{3.4}$$

$$\Rightarrow \tau = R_{\mathrm{Ch}} C_{\mathrm{Ch}}^{\mathrm{eff}} \approx 20\,\mathrm{ms}. \tag{3.5}$$

For calculating the total MCP capacitance he used the dielectric constant $\epsilon = 8.3$ for 8161 Corning glass. Assuming that most of the charge gets depleted from the last 20% of the channels he calculated the effective channel capacitance C_{Ch}^{eff}. In contrast to Tremsin (Equation 3.2), Wiza neglected the constant k. Without discussing the result one should keep in mind that the dead time τ is linear proportional to the channel plate resistance R_{Ch}.

Another possibility to evaluate the time resolved saturation is the ratio of strip current I_s and output current I_e. Tremsin [27] reported a limiting value for single MCPs (no Chevron configuration) of $I_e/I_s \approx 0.48$. Wiza [24] determined the limiting ratio to be 0.1 when operating the MCP as DC current amplifier. According to this imprecise information, the evaluation in this work will stick to an analysis using the channel plate resistance as determining parameter.

In contrast to the recharge time for single channels an MCP can achieve higher count rates when the incoming particles are distributed across the complete MCP surface. Similar to the subject of this thesis Kühnel et al. [28] presented measurements where MCP and readout electronics provide sufficient count rates at temperatures down to 25 K. Schecker et al. [29] received a none changing pulse height distribution for temperatures down to 14 K, using a standard gain model [30]. Nevertheless, the MCP performance is highly dependent on the incident rate and temperature. For coincidence measurements the MCP count rate has to suffice the small time difference of the incident events even if the event to detect has a small repetition rate itself.

3.2. MCP Detector Construction

In this work a MCP detector (construction principle see Figure 3.4) is tested. The detector uses a doubly stacked Chevron configuration. Relevant parameters for the two channel plates, produced by Photonis, are the open area ratio $OAR = 0.6$, the bias angle $\beta = (8 \pm 1)°$, the MCP quality diameter $D = 120 \, \text{mm}$, the MCP thickness of $(1.50 \pm 0.03) \, \text{mm}$, the channel diameter $d = 25 \, \mu\text{m}$.

A voltage gradient built up between the first electrode net and the
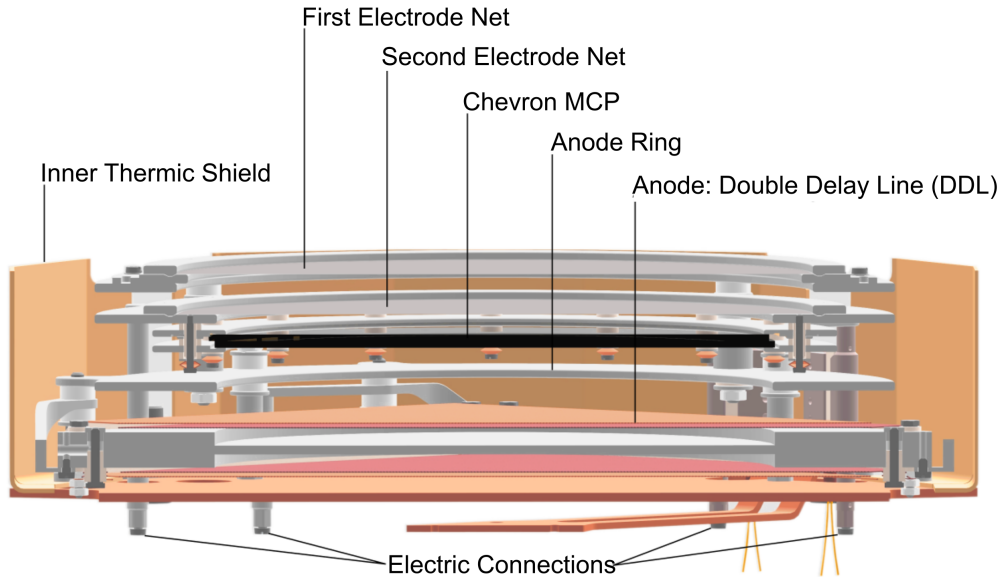

Figure 3.4.: Detector construction used in this work. The first electrode net marks the detector entrance. The two net electrodes, the Chevron electrodes (front- and backside independently) and the anode ring are electrically connected separately. Incident particles transmitted by the electrode nets collide with the channel walls of the MCP and produce a SEM reaction cascade. Emitted electrons travel towards the double delay line anode which consists of two alternately winded wires for the x- and y-direction. The inner thermic shield reflects incoming thermal radiation and makes sure that the detector can be operated at cryogenic temperatures.

MCP front face can accelerate incident particles parallel towards the MCP

surface normal. Dependent on the polarity of incoming particles the voltage gradient has to be chosen contrary to the particles charge. After the MCP front face the voltage gradient has to be positive, since from there on only secondary electrons are relevant. While the nets are of less importance in this work, they act as termination of the electric field applied inside the reaction microscope [8; 10]. To prevent short circuits each electrode ring is electrically separated by ceramic disks of different sizes. Since the detector is operated in ultra high vacuum and in cryogenic environment, the used materials need low outgassing-properties, low oxidation rates and high thermal stability. Screws have to be vented since gas inclusions could lead to local outgassing. The electrode rings are made of 1.4435 BN2-material, screws and other connectors of A4-steel[1], the thermic shields of highly pure copper, the wire of the double delay line of CuZr and the ceramics of Al_2O_3.

3.2.1. Cup Springs Counteracting the Consequence of Thermal Contraction

The different thermal expansion coefficients of the insulating ceramics and the A4-steel parts can lead to a problem during the cooling process. Thermal contraction may cause tension across the channel plate due to fabrication tolerances and local unevenness of different construction parts. The original construction had to be adapted and additional CuBe cup springs were integrated (see Figure 3.5). The length contraction for the different materials can be calculated according to Equation 2.13 using the thermal expansion coefficients $\alpha_{\mathrm{Steel}} = 16 \cdot 10^{-6}/\mathrm{K}$ for stainless steel and $\alpha_{\mathrm{Al_2O_3}} = 11 \cdot 10^{-6}/\mathrm{K}$ for the insulating ceramics. These used room temperature values are taken from the Solid Works data base and change during the cooling process. The relevant temperature range reaches from room temperature ($300\,\mathrm{K}$) to around $10\,\mathrm{K}$, yielding $\Delta T = 290\,\mathrm{K}$. The length of materials relevant for different contraction is $4.5\,\mathrm{mm}$ (see Figure

---

[1]Common stainless steel is called A2-steel. Compared to that, A4-steel contains a few percent of molybdenum to further improve its oxidation properties.
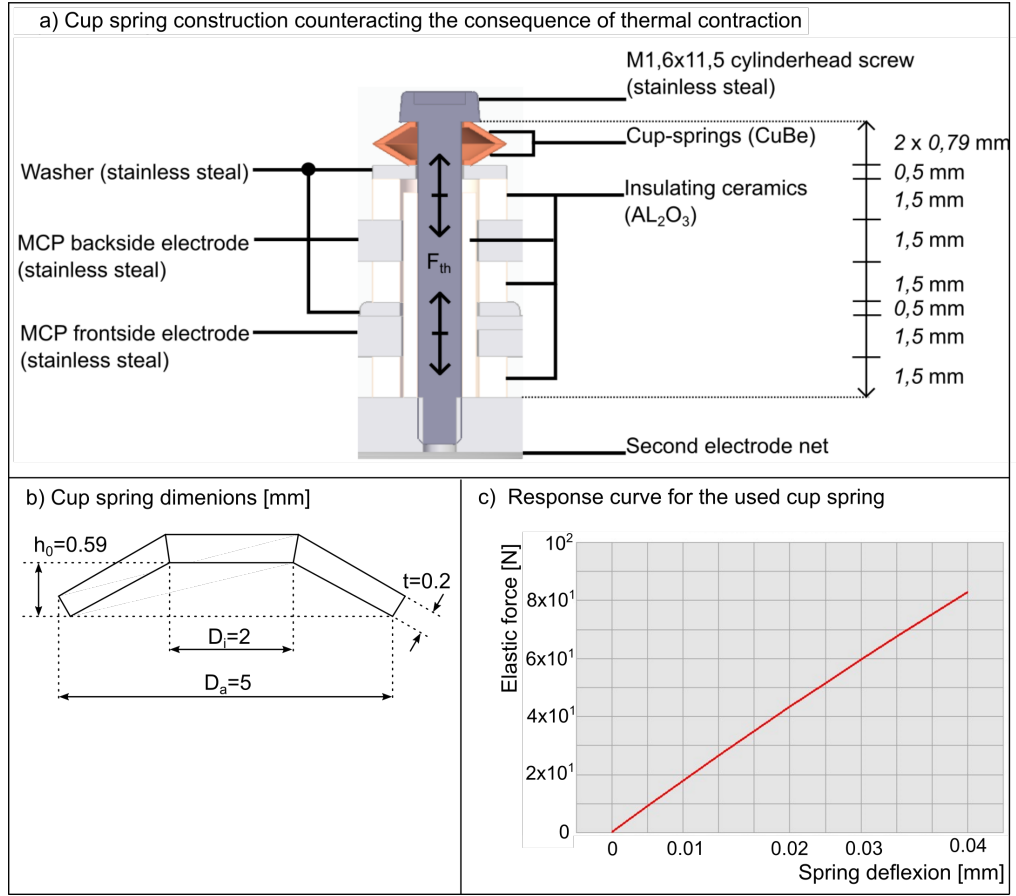
Figure 3.5.: Characteristics and working principle of CuBe cup springs, used to partially absorb the thermal contraction. a) Modified construction. The screw, the electrodes and the washers are made of A4 stainless steel, while the insulating ceramics are made of Al_2O_3. Due to different thermal expansion coefficients one has to oppose the change in length of a total of $4.5\,\mathrm{mm}$ ceramics to that of stainless steel. The cup spring provides a force counteracting to the thermal contraction F_{th}. b) Relevant parameters of the cup springs. c) Response curve, generated using [31]. The spatial dimensions used can be seen in (b), the Poisson number is 0.37, taken from the Solid Works data base.

3.5). These relevant parts are where the screw is surrounded by insulating ceramics.

$$\text{Stainless steel}: \Delta L_{\mathrm{screw}} \approx 21\,\mu\mathrm{m}, \tag{3.6}$$

$$Al_2O_3-\text{ceramics}: \Delta L_{\mathrm{ceramics}} \approx 14\,\mu\mathrm{m}. \tag{3.7}$$

Since the screw is contracting more than the ceramics, the cup-springs have to compensate a total length contraction of $\Delta L_{\text{tot}} \approx 7\,\mu\text{m}$. Comparing this result to Figure 3.5.c) the counteracting force per cup spring yields about $14\,\text{N}$. Using a total of 32 springs and considering the stacking of two springs per screw the final counteracting force results in $112\,\text{N}$.

3.2.2. Voltage Supply

To provide proper voltages (complete scheme shown in Figure 3.6) a first Voltage Distribution Box (VDB) is used respectively a voltage divider (circuit diagram see Appendix A). It distributes a single input voltage to separate, independent outputs supplying the MCP front and back electrode, the anode ring and the anode wiring. One uses a series of voltage dividers, its resistors were chosen such that a positive voltage gradient is built up from the MCP front face towards the anode. The first and second electrode net is contacted separately via two further voltage supplies. Thus, the voltage gradients accelerating incoming particles and SEM electrons are decoupled such that the detector can be used for positively or negatively charged particles. Also, the voltage applied to the first electrode net can be chosen freely such that it can be adapted to the electric field gradient inside the reaction microscope [8; 9; 10].

The Double Dealy Line (DDL) anode consists of one long, alternately winded signal and reference wire, both for x- and y-direction. The delay line-outputs of the first box are connected to a second VDB (circuit diagram see Appendix A) where the four inputs (X_{Signal}, $X_{\text{Reference}}$, Y_{Signal} and $Y_{\text{Reference}}$) are split into eight outputs, two for each input (for example $X_{1,\text{Signal}}$ and $X_{2,\text{Signal}}$). These outputs are connected to the wires of the double delay line where $X_{1,\text{Signal}}$ and $X_{2,\text{Signal}}$ denote the starting respectively ending point of the signal-wire in x-direction. A correct connection of signal and reference in- and outputs is important, because VDB 1 provides slightly higher voltages to its signal outputs $X_{1,1}$ and $Y_{1,1}$. Thereby, one achieves that more SEM electrons collide with the signal wires. The final signal outputs of the second VDB X_1, X_2, Y_1 and Y_2 denote noise free, decoupled, low voltage subtraction signals $X/Y_{1/2} = X/Y_{1/2,\text{S}} - X/Y_{1/2,\text{R}}$. Now "Signal" and "Reference" is abbreviated by "S" and "R". These signals are used for data acquisition.
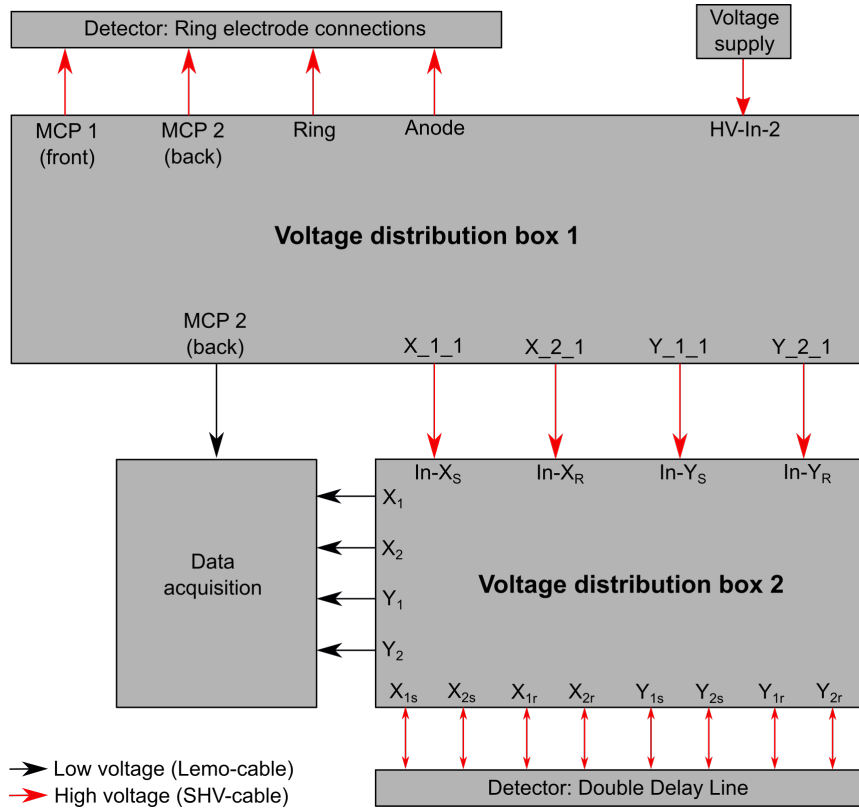
Figure 3.6.: Used voltage distribution principle. A high voltage supply is connected to the HV-In-2 connector of Voltage Distribution Box 1 (VDB 1). Using a series of voltage dividers, the input voltage is fractionized (circuit diagram see appendix A). While the ring electrodes of the detector are connected directly to VDB 1, the double delay line needs a second VDB. This box guides its four inputs to eight outputs by splitting up one input into two identical outputs (circuit diagram see appendix A). One connects the two ends of one signal (i.e. $X_{1,S}$ and $X_{2,S}$) and one reference wire (i.e. $X_{1,R}$ and $X_{2,R}$) of the double delay line for x- and y-direction. During measurements these outputs also act as signal inputs. The decoupled subtraction signals $X/Y_{1/2} = X/Y_{1/2,S} - X/Y_{1/2,R}$ are further processed in the data acquisition. The lowered voltage signal of one of the two MCP electrodes is needed for triggering the data acquisition.

The complete voltage distribution scheme can be seen in Figure 3.6. The separate voltage supplies for the detector nets are not shown. For wiring

the double delay line it is necessary to use a twisted pair configuration[2] connecting related ends of signal and reference wires. Thereby the influence of external high frequency signals can be minimized with low effort.

3.3. Readout Technique and Data Acquisition

In the following, the generation of a two dimensional image, extracted from the electrical signals thumbed at the two ends of each wire, will be discussed. For simplification it will only be referred to one exemplary DDL wire.

The SEM electron cloud emitted from an MCP channel collides with the wire of the DDL. Due to the clouds spatial extent more than one winding can be hit. The electrons absorbed by the wire produce an electric pulse traveling to both wire ends (see Figure 3.7). Due to broadening effects caused by dispersion[3] the signals do not consist of separate pulses for numerous wires hit by the electron cloud emitted by one MCP channel for one SEM reaction cascade. The outgoing signals are in the first instance processed in VDB 2. The inductive decoupling produces a positive signal according to $X/Y_{1/2} = X/Y_{1/2,S} - X/Y_{1/2,R}$. Hence, background noise is prevented and the carrier voltage becomes zero.

Since the used amplifier Ortec FTA 820 only processes negative signals, an inverter is added after VDB 2. The amplified signals are further processed with an Analog Digital Converter ADC, provided by RoentDek. The four signals $X_{1/2}$ and $Y_{1/2}$, as well as the MCP signal define the inputs of the ADC. During a reaction cascade inside a MCP channel, charge is depleted of the channel wall. Thus, the voltage drops for the duration of the SEM cascade and is restored by the voltage supply. This voltage drop is the origin of the data processing, it is used as group trigger for the delay line channels. Once the MCP-signal intersects the trigger threshold at time $t_{\text{Trigger}-1}$ a time window $[t_{\text{Trigger}-1} - 14.4\,\text{ns}; \; t_{\text{Trigger}-2} + 19.2\,\text{ns}]$ is opened to sample the delay line channels, whereas the positive time limit is determined after the MCP signal falls below the trigger threshold at time $t_{\text{Trigger}-2}$ again.

---

[2]A twisted-pair-configuration is simply achieved by twisting the cables.

[3]Similar to laser pulses in refractive media, electrical pulses suffer from dispersion effects. Different frequencies experience different drift velocities and the pulse broadens as the signal "collects" additional group delay dispersion during propagation.
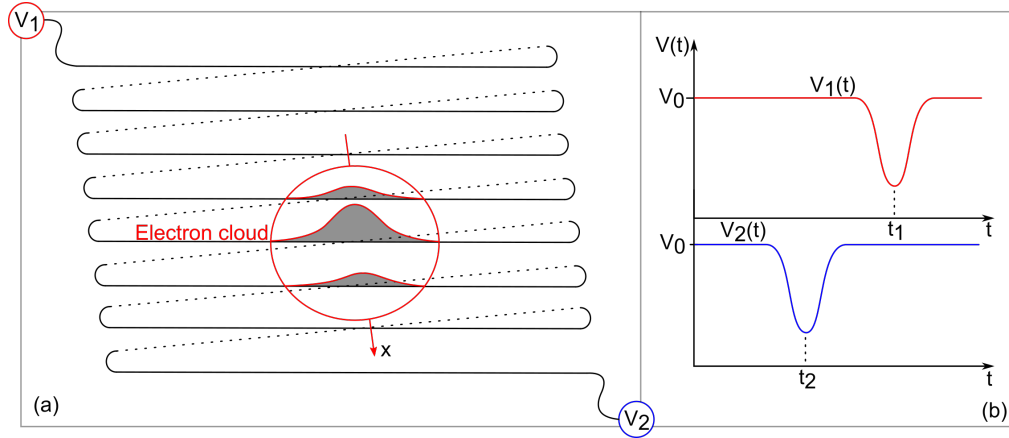
Figure 3.7.: Working principle for the production of signal pulses for a single DDL wire. (a) The electron cloud hitting the wire produces an electrical pulse traveling to both wire ends where the signals V_1 and V_2 are thumbed. (b) Before the decoupling, the carrier voltage equates to the voltage V_0 applied to the DDL. In the analysis each pulse is assigned to the time $t_{1/2}$ which refers to its electrical propagation time.

In this time window all incoming and already digitized signals are saved if their amplitude is higher than their individual trigger threshold which can be set for each channel independently. For each signal the amplitude A and its point in time t_s with respect to the calculated time of the MCP voltage drop t_{MCP} is determined as shown in Figure 3.8. Using the time sum condition

$$t_{\mathrm{x/y},1} + t_{\mathrm{x/y},2} = \mathrm{const}, \tag{3.8}$$

one can assign related signals. The spatial representation is finally calculated by:

$$X/Y = f_{\mathrm{x/y}} \cdot \left(t_{\mathrm{x/y},2} - t_{\mathrm{x/y},1} \right), \tag{3.9}$$

with the proportionality factor $f_{\mathrm{x/y}}$ which represents the vertical drift velocity for signals on the delay line.

In case of lost signals, one can fall back to different reconstruction algorithms using the time sum. Also two MCP signals which are produced by coincident particles, can be separated by a deconvolution algorithm, as long

as the Rayleigh limit $\Delta t \geq 1.22 \cdot$FWHM is fulfilled where Δt is the temporal separation of the two timestamps and FWHM describes the larger of the two Full Width Half Maxima of the signals. Due to the mostly qualitative scope of this work, the shown analysis is sufficient. For experiments using a reaction microscope further reconstruction principles will potentially become important, more detailed information can be found in the Ph.D. theses of Senftleben [32], Schnorr [33] and Pflüger [34]. Although they used a different data acquisition system, the principle of various reconstruction algorithms can be integrated to various data acquisitions.
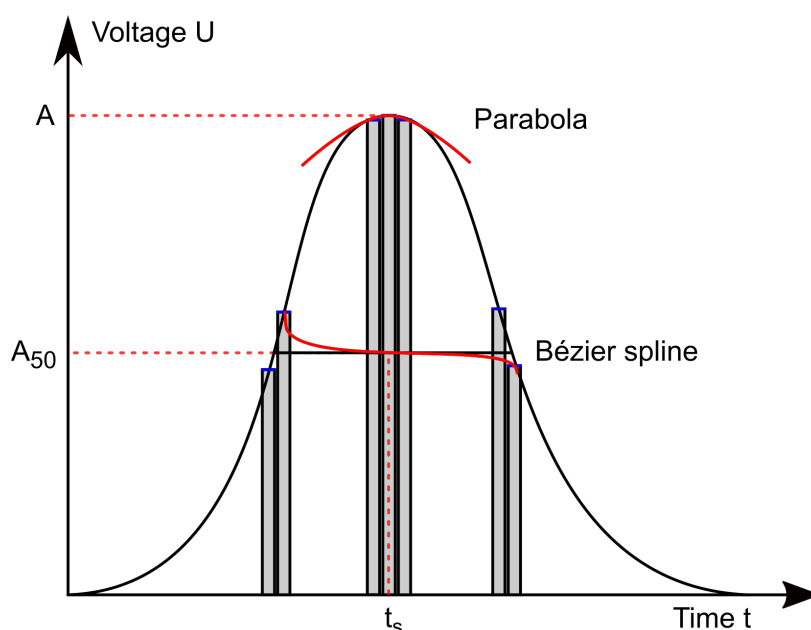

Figure 3.8.: Schematic of signal processing. After digitizing an incoming pulse, it is in a first instance characterized by three parameters: the maximum amplitude of the signal A, $A_{50} = A/2$ and the time t_s. The amplitude is determined by the maximum of a parabola, fitted to the three highest bins of the signal. The second step is calculating A_{50}. The four nearest signal bins of A_{50} define a Bézier spline which intersection with the A_{50}-line yields the signal's point in time t_s. Since real signals can look much more jittery than shown here, it is more reliable to use the Bézier spline to determine a timestamp than just to use the maximum of the fitted parabola.

4. Experimental Setup

The setup inside the vacuum chamber is shown in Figure 4.1. Each flange with diameter $d \geq 40\,\text{mm}$ is sealed with viton o-rings, suitable for pressures down to $10^{-10}\,\text{mbar}$. To achieve temperatures in the few Kelvin regime i.e. to isolate the detector from ambient thermal radiation two thermic shields are installed and thermally connected to the two stages of the coldhead. The shields are made of high purity copper which has an emissivity ϵ of 0.02 (polished) to 0.05 (untreated, shining). Incident black body radiation, caused by construction parts at room temperature ($T_0 = 300\,\text{K}$), transfers heat to the system. The heat input reads:

$$\dot{Q} = \kappa_\text{B}\epsilon_\text{s}A_\text{s}\left(T_0^4 - T_\text{s}^4\right), \tag{4.1}$$

with the emissivity ϵ_s, the Stefan Boltzmann constant $\kappa_\text{B} = 5.67\,\text{W}^2/\text{m}^2\text{K}^4$, the actively reflecting area A_s and the temperature T_s of the shield. Assuming $T_\text{s} = 30\,\text{K}$, using $\epsilon_\text{s} = 0.05$ and $A_\text{s} = 0.2\,\text{m}^2$ it yields $\dot{Q} \approx 4.6\,\text{W}$. By comparing this result to the capacity map (see Figure 4.2), provided by Sumitomo, one sees that the beforehand used assumption of $T_\text{s} = 30\,\text{K}$ is valid. When the temperature of stage 2 is in the region of a few Kelvin, the outer shield (thermally equivalent to stage 1) is cooled with a power of around $5\,\text{W}$ at $30\,\text{K}$. This leads to an equilibrium between input heat and cooling power and the temperature of the shield stays constant. When the shield reaches sufficiently low temperatures, single constituent elements of air start to condensate e.g. nitrogen condensates at surrounding conditions of $77\,\text{K}$ and $1\,\text{bar}$[1]. This condensate layer influences the emissive properties of thermic shields and can increase the external heat input [36]. Additionally to the copper shields themselves, the lower part of the outer shield is wrapped with multilayer insulation (10 layers). This further improves the emissive properties and therefore decreases external heat input. In

---

[1]With decreasing pressure the condensation temperature decreases. Please find the p-T-diagrams for a couple of elements and molecules in Day [35].
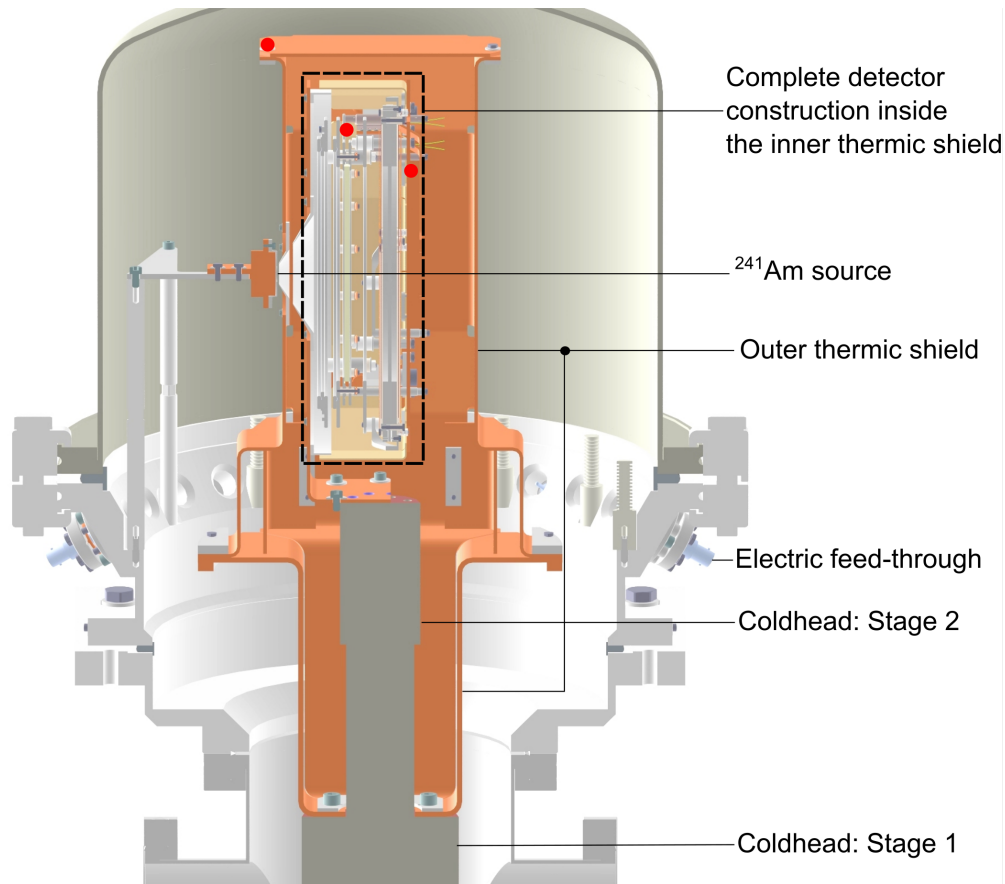
Figure 4.1.: Profile of the measurement setup. The coldhead is fixed on the bottom of the vacuum chamber. The outer thermic shield is mounted on stage 1 of the coldhead while the inner thermic shield is mounted on stage 2. Hence both shields are in thermal equilibrium with the respective stage. The detector is located inside the inner shield. The $^{241}_{95}$Am-source is mounted separately on a non-shielded attachment and stays unaffected by the cryo temperature. The positions of three Si-diodes for temperature measurements is marked with red spots.

Equation 4.1 only the copper parts without multilayer insulation are taken into account.

Pt1000 elements, type K thermocouples and Si-diodes are used for temperature measurements. One Pt1000 and one thermocouple is mounted at
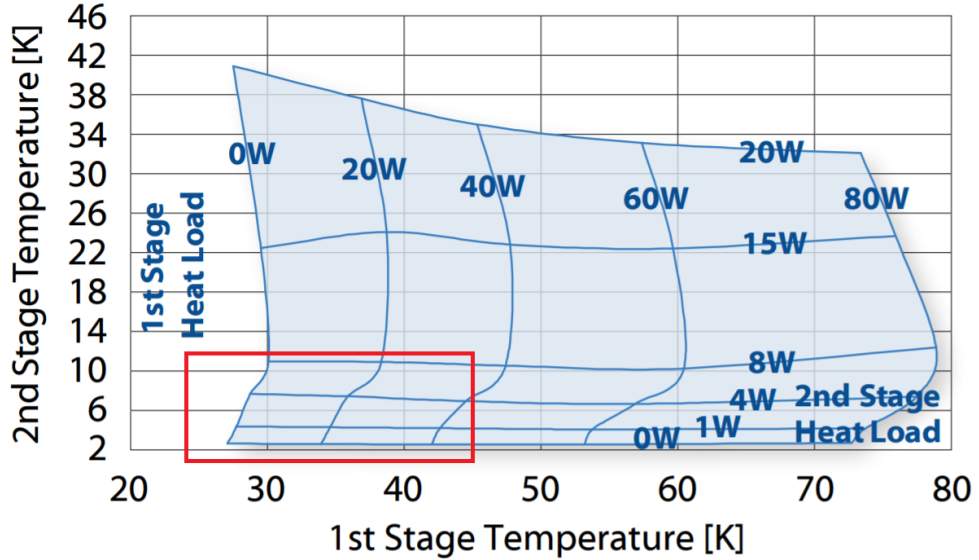
Figure 4.2.: Capacity map of the coldhead model RDK-408D2, produced by Sumitomo, at 50 Hz-operation, taken from [37]. The horizontal lines describe the heat pumping power of stage 2, the vertical lines the heat pumping power of stage 1. The x- and y-axis shows the temperature of stage 1 and stage 2, respectively. The pumping powers of the two stages are strongly correlated, e.g. it is not possible to cool one stage independently. The region of interest is marked in red, desirable temperatures would be 30 K at stage 1 and 10 K at stage 2.

the top of the outer shield and one of each of these three types on the foot of the inner shield which is directly screwed to the second stage of the coldhead. One further thermocouple is mounted on the frontside of the source holder and one further Si-diode is placed on the MCP frontside electrode. By this extensive use of sensors the temperature of all relevant parts of the experimental setup can be tracked. Due to the high precision of Si-diodes in the cryogenic temperature range, most temperatures presented in this work are taken from these sensors. For sufficient thermal conductivity between different construction parts which belong to the same thermal stage each

contact point is coated with a thin layer of Apiezon N. This film provides reliable thermal contact of separate parts.

4.1. List of Used Devices

Purpose	Device	Comment
Fore-Vacuum Controller	Leybold IoniVac IM 540	
Fore-Vacuum Gauge	Leybold Thermovac TTR 91 NS	Used twice, $p_{min} = 3.8 \cdot 10^{-4}\,\text{mbar}$
UHV-Controller	Vacom ATMIGRAF	
UHV-Gauge	Vacom ATMION	$p_{min} = 1 \cdot 10^{-10}\,\text{mbar}$
Turbo Controller	Pfeiffer DCU 110	Used for HiPace 80
Turbo Pump	Pfeiffer HiPace 80	
Turbo Controller	Pfeiffer DCU 310	Used for HiPace 300
Turbo Pump	Pfeiffer HiPace 300	
Fore-Vacuum Pump	Edwards nXDS6i	
Coldhead	Sumitomo RDK 408 D2	Stage 1: $40\,\text{W}$ @ $43\,\text{K}$ Stage 2: $1\,\text{W}$ @ $4.3\,\text{K}$
Compressor	Sumitomo CSW 71	
Temperature Controller	CryoCon 24 C	
Si-Diode	CryoCon S950	Used threefold for temperature measurement
Amplifier	Ortec FTA 820	Gain $G = 200$
High Voltage Supply	NHQ 204 M (2x) NHQ 206 L (1x)	
Voltage Supply	Rhode & Schwarz HMP 4040	Used for heating resistor
Oscilloscope	Rhode & Schwarz RTM 3004	
Data Acquisition	RoentDek FADC 8B/10-2	

Table 4.1.: List of used devices.

4.2. Alpha Source and Effective Solid Angle

The particle source is $^{241}_{95}$Am with an activity of $A_0 = 37\,\text{kBq}$ at the production day (7th December 1971). Its primary decay path with a half life of $T_{1/2} = 432.6$ a [38] is:

$$^{241}_{95}\text{Am} \rightarrow {}^{237}_{93}\text{Np} + \alpha\ (+\gamma),\tag{4.2}$$
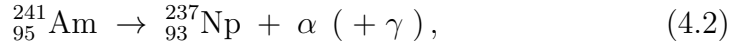
where α and γ describe a $^4_2$He-core and a photon, respectively. With a probability of 85% an energy of 5.486 MeV is released. Additionally to the alpha particle in most of these reactions one or more gamma quanta are produced. Using the decay law

$$\frac{\mathrm{d}N}{N} = -\lambda\mathrm{d}t,\tag{4.3}$$

one can determine the activity in the year 2020 to be

$$A(t) = A_0 \exp\left(-\frac{\ln(2)}{T_{1/2}}t\right) = 34.2\,\text{kBq},\tag{4.4}$$

emitted into a solid angle of 4π. In the next step the effective solid angle of the MCP is calculated. The distance between source and MCP is $x = 39\,\text{mm}$ and the effective MCP radius is $a = 55\,\text{mm}$ (see Figure 4.3). Assuming a pointlike source the half apex angle of the included cone is $\alpha = 0.954\,\text{rad}$. Thus the effective solid angle Ω reads

$$\Omega = 2\pi\left(1 - \cos(\alpha)\right) = 2.649\text{ sr}.\tag{4.5}$$

Hence, the effective rate of emitted alpha particles, seen by the MCP, results to

$$A_{\text{MCP}} = 7.22\,\text{kBq}.\tag{4.6}$$

In reality the source has a diameter of 7 mm and hence a spatial extent, this can slightly increase the effective solid angle and the calculated effective activity. Also the emitted photons and provoked ions from the MCP front face can produce SEM cascades and have to be taken into account. In contrast to that the transmission of the electrode nets and the OAR of the detector decrease the measured rate.
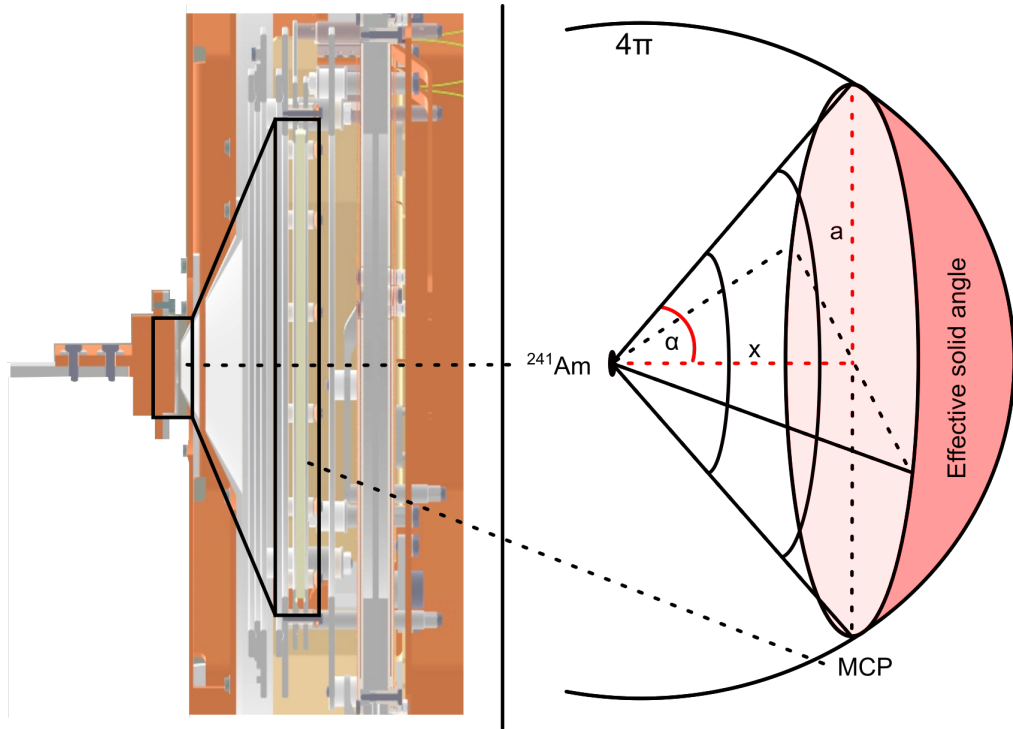
Figure 4.3.: Determination of the relevant solid angle. The distance between the MCP and the $^{241}_{95}$Am-source is $x = 39\,\text{mm}$, the MCP has an active radius of $a = 55\,\text{mm}$. This yields the half apex angle of $\alpha = 0.954\,\text{rad}$.

4.3. Thermal Connection towards the MCP

In this section two optimizations of the thermal connection towards the MCP are discussed. These changes to the original setup lower the minimally reachable MCP temperature to 35 K. Additionally, possibilities for further optimization are presented.

During the process of building up the setup, it became clear that the thermal connection between the second stage of the coldhead and the detector is insufficient. The only direct connection between the baseplate of the detector and the coldhead is made up of four screws out of stainless steel (see Figure 4.4). These stainless steel-copper junctions are inappropriate to transport enough heat from the detector towards the coldhead which yields a

low effective cooling power. After four days of cooling, the baseplate adapted to a temperature of 33 K while the second stage equilibrated at 6.5 K after one day of cooling. Additionally, there are further steel-ceramic-junctions (separating the different detector modules, see Figure 3.4) decreasing the effective cooling power for the MCP. Of course, the setup will equilibrate at some point but to provide measurement results within proper times the timescale of cooling down the detector had to be lowered.
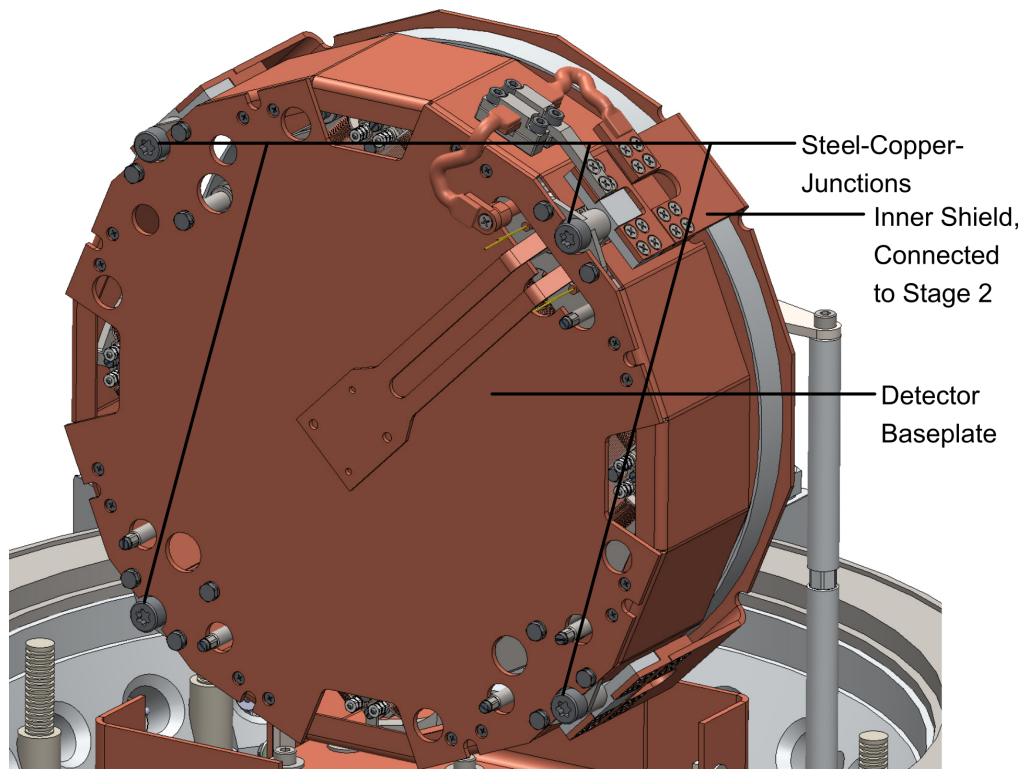

Figure 4.4.: Construction of the inner shield including the detector. The four stainless steel screws, marked as "Steel-Copper-Junctions", define the only direct connection between the second stage and the detector baseplate before the improving copper braid construction (see Figure 4.5) is added.

To improve the thermal conductivity between the MCP and the coldhead a copper braid is added. It thermally connects the part of the inner thermal shield which is directly mounted to the coldhead, and the MCP front face electrode (see Figure 4.5). Due to the high voltage difference between the

MCP electrode and the thermal shield (ground potential) both have to be electrically decoupled. Therefore, a sapphire crystal[2] is added between the two parts of the braid (see Figure 4.5) such that electrical safety can be guaranteed. It is also important that different parts of the additional construction have to be connected using surfaces which are as large as possible. A bigger contact surface increases the thermal conductivity between single parts.
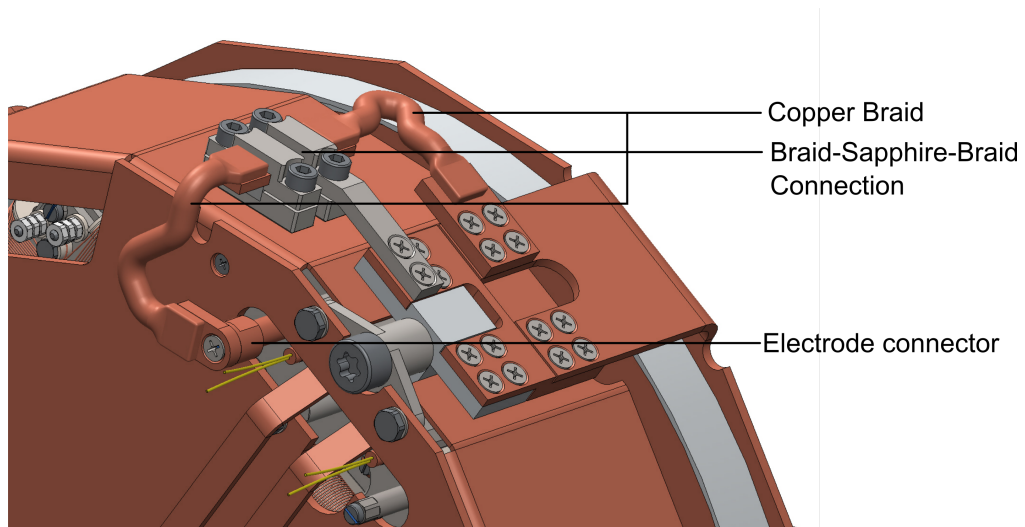

Figure 4.5.: Improving the thermal conductivity between the second stage and the channel plate. For best possible results the electrode connector and the screw fixing the lower part of the braid is produced out of copper instead of A4-steel. To achieve the electric decoupling two single braid parts are separated by a sapphire. The lower part of the braid which is electrically contacted to the MCP electrode has to be isolated by numerous short ceramic pipes to prevent direct electrical contact to other construction parts. The upper part of the braid was redesigned to a solid copper part before the measurements were executed.

After an additional temperature sensor has been added to the MCP front face electrode using a cryo-suitable epoxy adhesive (Stycast FT 2850 combined with the Stycast Catalyst 9), the temperature was recorded during the cooling process. The measured temperatures and MCP resistances of

---

[2]Artificial sapphires have a very high thermal conductivity and act electrically as insulators.

the first cooling process with copper braid is shown in Figure 4.6. The MCP resistance is determined using a voltage divider. A resistor with $R_{\mathrm{in}} = 500\,\mathrm{k\Omega}$ is connected in parallel to the MCP stack and a supply voltage of $U_{\mathrm{in}} = 500\,\mathrm{V}$ is applied. By measuring the dropped voltage U_{out} of the additional resistor the MCP resistance can be calculated:

$$R_{\mathrm{MCP}} = R_{\mathrm{in}} \left(\frac{U_{\mathrm{in}}}{U_{\mathrm{out}}} - 1 \right). \tag{4.7}$$
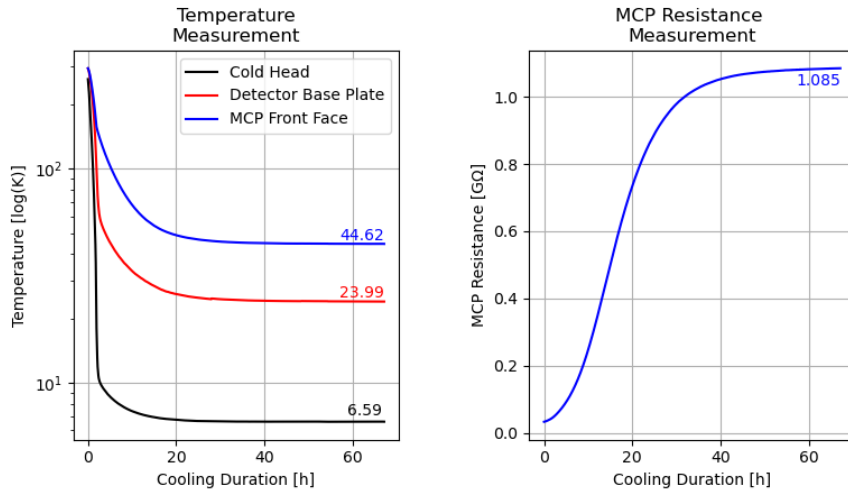

Figure 4.6.: Temperatures at different positions (left) and MCP resistance (right) during the first cooling process after installing the Cu-braid. The left side shows the temperatures at the MCP front face electrode (blue), at the detector base plate (red) and on top of the second stage of the coldhead (black). Since the material inside the inner shield has to be as cold as possible, the blue curve is most relevant. At the end of the curves the final temperatures are shown as displayed by the temperature controller. The precision of the temperature measurement is $0.5\,\mathrm{K}$. The minimal temperature reached at the MCP front face is $44.62\,\mathrm{K}$. The right side shows the calculated MCP resistance (Equation 4.7) using $U_{\mathrm{in}} = 500\,\mathrm{V}$ and $R_{\mathrm{in}} = 500\,\mathrm{k\Omega}$. From this one can see that for the final MCP front face temperature the MCP resistance is measured to be $1.1\,\mathrm{G\Omega}$.

Since the final temperature at the MCP front face after more than $60\,\mathrm{h}$ of cooling was measured[3] to be $44.62\,\mathrm{K}$, further improvements had to be made.

---

[3]The precision of the temperature measurement is $0.5\,\mathrm{K}$. The discussed values are taken as displayed by the temperature controller.

The lowest possible temperature without changing the MCP construction was measured by disconnecting all cables and closing the hole for particle insertion in the outer shield using super isolation (Figure 4.7).
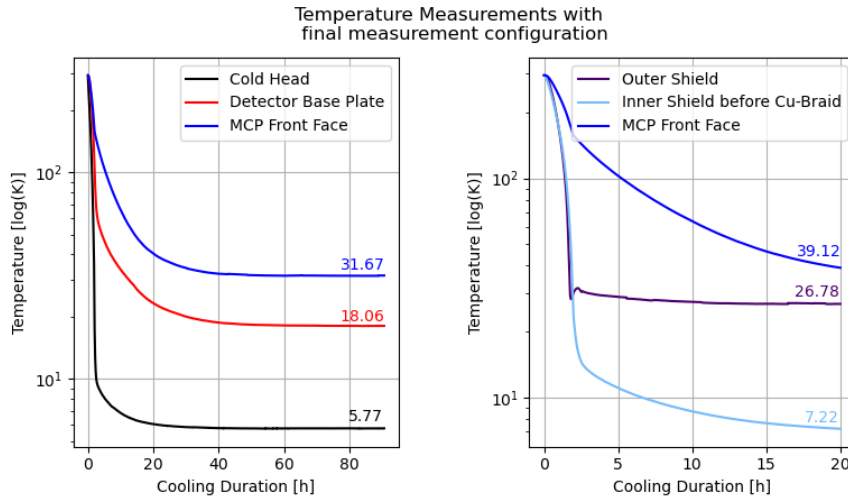

Figure 4.7.: Temperatures at different positions during the cooling process without cable connections or heat radiation through the hole for particle insertion. In comparison to the previous measurement with wiring and particle source (see Figure 4.6), the final measured temperature at the MCP front face has been lowered by 13 K to 31.67 K. One can see on the right side that the temperature of the MCP front face electrode in the first 20 h of cooling is approaching the temperature of the outer shield. The temperature of the inner shield at the position where the copper braid construction is mounted (see Figure 4.5, right before the upper part of the braid) can be measured to be 7.22 K after 20 h of cooling. Since the goal of the measurement on the right was to check that the light blue curve approaches the black curve on the left, it was stopped after 20 h.

Without any heat input from cables or radiation through the hole for particle insertion the final temperature of the MCP front face electrode after more than 90 h of cooling is measured to be 31.67 K. Therefore the previously used 0.6 mm Capton coated Cu-cables are exchanged by 0.36 mm capton wrapped Cu-cables. The displayed temperatures for this final setup are shown in Figure 4.8.
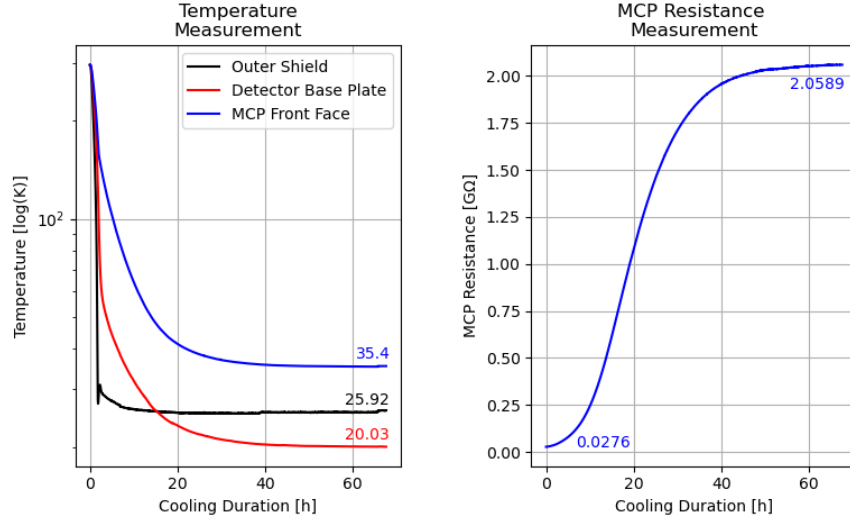
Figure 4.8.: Displayed temperatures at different positions (left) and MCP resistance (right) using the final setup including the α−source, changed wiring and copper-braid. The MCP temperature during the measurements is in the following assumed to be $35\,\mathrm{K}$. The final MCP resistance is determined to be $2.059\,\mathrm{G\Omega}$ while the room temperature resistance (first displayed MCP resistance) was measured to be $27.6\,\mathrm{M\Omega}$.

Comparing the values MCP resistance and temperature to a similar measurement carried out at the MPIK the results are reasonable [28] because the resistance increase and the temperature change are in the same order of magnitude. It can be assumed that the temperature measured at the MCP front face electrode is in equilibrium with the complete channel plates.

5. Detector Characterization

Before starting a measurement it is important to detach the high-vacuum-gauge to prevent signal noise. Furthermore, the source holder must not have physical contact to the outer shield. Otherwise the Am-source adapts to the temperature of the outer shield and may shiver. The channels 1-5 (CH01 - CH05) of the data acquisition hardware are identified as the following: CH01 for X1, CH02 for X2, CH03 for Y1, CH04 for Y2, CH05 for the MCP. Although the data acquisition software, called Cobold, and its ADCs (Analog Digital Converters) basically work like an oscilloscope, the displayable voltage is restricted to $\pm 1000\,\text{mV}$. This often leads to problems during a measurement. When the MCP is working near saturation (high supply voltages), anode and MCP signals often peak at voltages above the limit set by the software and the quality of the resulting image is low due to false coincidences between individual channel signals. Therefore, the detectors can not be operated near saturation if detailed images are needed.

During measurements the measured rate of incident particles is in the order of $7\,\text{kHz}$ but depends on the supply voltage. Slowly propagating ions, provoked inside the source are measured near (X,Y)=(0,0), since they are accelerated perpendicularly towards the MCP surface after being ejected of the source (see Figure 5.1). Setting the voltage of the first net to a small positive value leads to an image without the centered maximum, because slow ions are repelled before of the first net due to their positive charge. The bulge on the edge in the shown image (Figure 5.1) are the result of an electric field between mounting screws, electrically connected to the second net, and the anode voltage. Without applying a voltage to the second net, the local voltage gradient influences the trajectory of the electron cloud after its emission from the MCP channel.
On the outer edges of the image small cutoffs are visible. This is due to the spatial limitation of the DDL (Double Delay Line). The interference-like spatial structure of the image may be the result of the superposition of the

two nets. The consecutive transmission of two periodic structures produces a Moiré pattern if the structures are not aligned perfectly. A small rotation of the first net with respect to the second net can produce the slight spatial modulation.
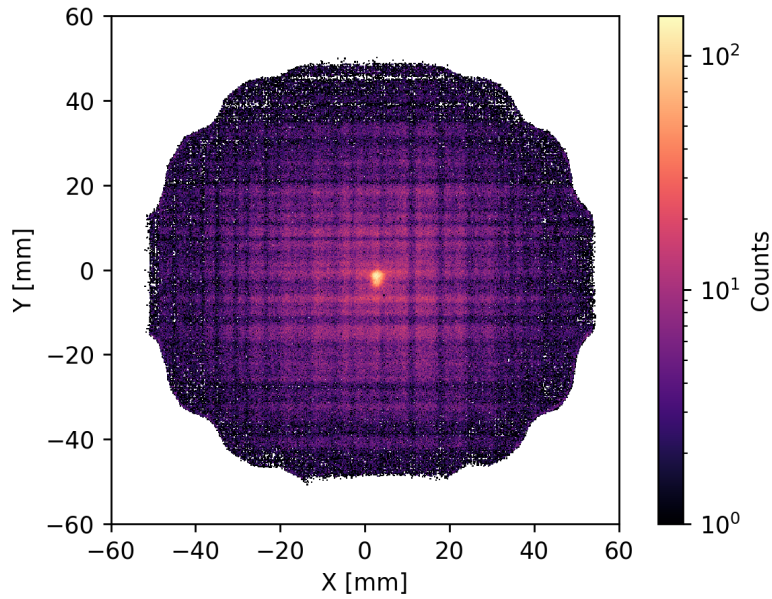

Figure 5.1.: Full detector image with the following measurement parameters. Temperature: 300 K; Supply Voltage at HV-in-1 of VDB 1: -2750 V; Attenuation for CH05: 13 dB; nets: floating; Trigger: -110 mV for CH01, -100 mV for CH02, -110 mV for CH03, -110 mV for CH04, -50 mV for CH05; number of measured events: 1 000 000. A maximum near (0,0), produced by slow ions provoked from the source, can be seen. On the four outer edges the cut-off due to the spatially restricted DDL, as well as the slight Moiré pattern can be observed. A more detailed evaluation of the different effects can be found in the text.

5.1. Saturation Properties

The measurement parameters in this section are shown in Table 5.1. The PHD of all MCP signals is displayed for three different voltages to evaluate the saturation properties of the used channel plates (see Figure 5.2-5.3.)

Parameter	Value
Temperature	35 K and 300 K
Supply Voltage	$-2700\,\mathrm{V}$, $-2900\,\mathrm{V}$ and $-3100\,\mathrm{V}$
Attenuation	CH05: -12dB before Amplifier
	50% damping for each ADC-input
Detector Nets	floating
Triggers	CH01: $-120\,\mathrm{mV}$
	CH02: $-120\,\mathrm{mV}$
	CH03: $-120\,\mathrm{mV}$
	CH04: $-120\,\mathrm{mV}$
	CH05: $-80\,\mathrm{mV}$
Number of Measured Events	1 000 000

Table 5.1.: Measurement parameters for the MCP saturation measurements. The supply voltage is connected to the HV-IN-1 connector of VDB 1; it should not be set equal to the voltage gradient between the two MCP surfaces.

As can be seen in Figure 5.2 the PHD at room temperature forms a clear maximum and broadens with increasing voltages. For a supply voltage of $-2700\,\mathrm{V}$ the PHD decays nearly exponentially. A small maximum for low trace maxima can be identified but can not clearly be distinguished from the underground. With increasing voltage the distribution peaks and becomes more symmetric and Gaussian-shaped. Qualitatively, it can be assumed that the MCP is operated near the saturation limit for a supply voltage of $-3100\,\mathrm{V}$.

Comparing the room temperature PHDs to the ones measured at 35 K (see Figure 5.3) the curves for saturated operation (red, $-3100\,\mathrm{V}$) can not be distinguished. The saturation operation stays unchanged. A difference can be seen for the supply voltages of $-2700\,\mathrm{V}$ and $-2900\,\mathrm{V}$. Qualitatively,
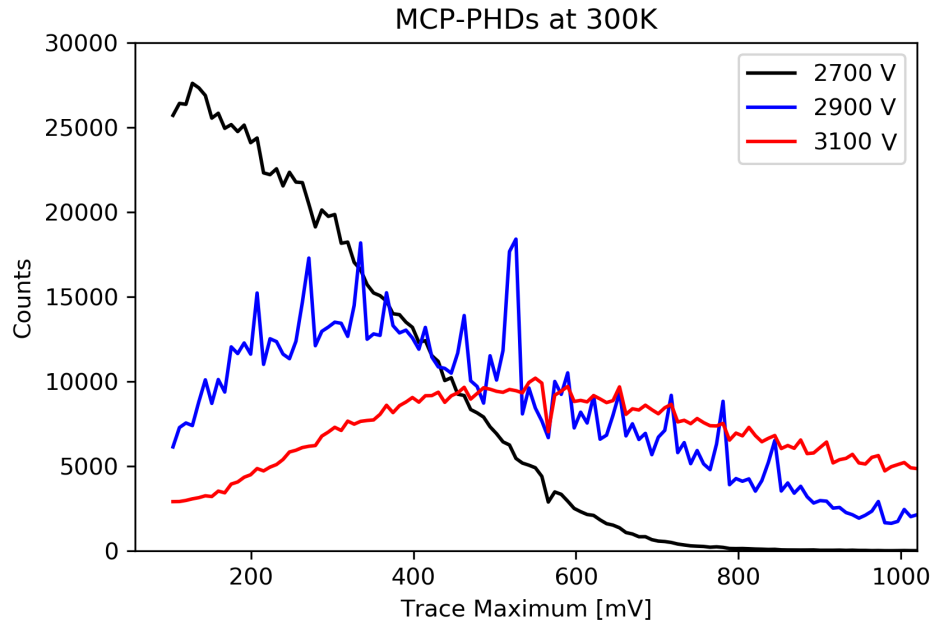
Figure 5.2.: PHDs of accumulated MCP signals for different supply voltages at room temperature. The measurement parameters are shown in Table 5.1. It gets clear that the distribution broadens and becomes Gauss-shaped with increasing supply voltages. It can be assumed that the MCP is operated near the saturation limit for a supply voltage of $-3100\,\text{V}$. For $-2700\,\text{V}$ the PHD decays nearly exponentially, a maximum is starting to form near the trigger threshold of $-80\,\text{mV}$. The blue curve shows an intermediate step between unsaturated and saturated MCP operation. The wiggling of the PHDs is due to the binning in the evaluation script and could not be corrected easily.

it seems like the PHDs at $35\,\text{K}$ form a clearer maximum for a smaller supply voltage. The MCP seems to reach the saturation operation for smaller supply voltages.

One possible explanation for this behavior is the increasing channel recharge time τ, discussed in Section 3.1.3. Particles hit the MCP with a constant rate. Due to the higher recharge time of the channel walls at $35\,\text{K}$, the probability grows that a SEM reaction cascade is produced in a channel, whose walls are not fully repopulated with electrons. Indeed,
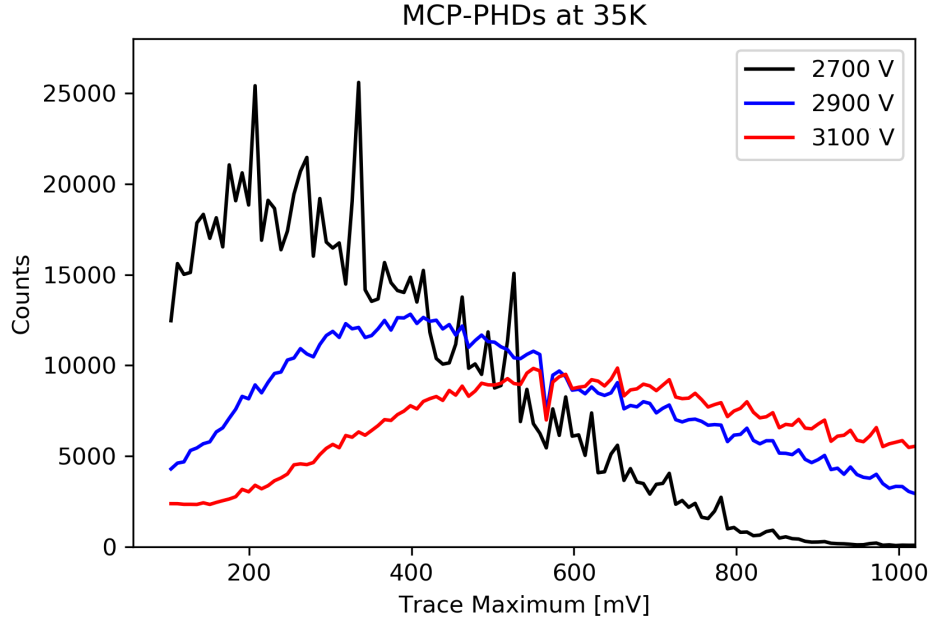
Figure 5.3.: PHDs of accumulated MCP signals for different supply voltages at a temperature of 35 K. The measurement parameters are shown in Table 5.1. The general properties of the PHDs stay unchanged compared to the measurement at room temperature (Figure 5.2). The black curve clearly differs to the previous measurement, it forms no clear peak near the trigger threshold of −80 mV. However, the blue curve looks much clearer and is close to form a symmetric maximum. It can be assumed that for 35 K the MCP is saturated at slightly smaller supply voltages than at room temperature.

this leads to measurable events but the resulting signal will have a smaller peak since less charge is emitted from the channel end. Therefore, even for smaller supply voltages the MCP operates in a saturated manner. It should be mentioned that the measurement rate shown by the data acquisition software Cobold remained unchanged after cooling down to 35 K. This also indicates a perfectly working channel plate, only the PHDs show small differences.

5.2. Detector Linearity

In this section the imaging capabilities of the MCPs are tested. A hole-containing mask is mounted in front of the first net such that the transmitted particle image is detected. The mask has a total of 730 bores with a diameter of $1\,mm$ and a nearest neighbor mid-to-mid-distance of $4\,mm$. Due to the angular illumination a small fraction of them is effectively used for imaging. It has to be checked whether possible irregularities in the DDL or the MCP structure cause deviations between the linearly structured object and the image. Table 5.2 shows all necessary measurement parameters.

Parameter	Value
Temperature	$35\,K$ and $300\,K$
Supply Voltage	$-2700\,V$
Attenuation	CH05: -13dB before Amplifier
Detector Nets	Net1: $200\,V$
	Net2: $-1000\,V$
Triggers	CH01: $-140\,mV$
	CH02: $-130\,mV$
	CH03: $-140\,mV$
	CH04: $-120\,mV$
	CH05: $-50\,mV$
Number of Measured Events	$500\,000$

Table 5.2.: Measurement parameters for the linearity measurement. The supply voltage is connected to the HV-IN-1 connector of VDB 1, it should not be set equal to the voltage gradient between the two MCP surfaces. The voltage applied to net 1 prohibits the appearance of an intensity maximum at the image center. Therefore, the hole structure can be resolved more exactly. The triggers are chosen independent of the previous measurement because in this section the image quality has to be optimized.

Figure 5.4 shows the detector image taken at room temperature. The linear structure of the hole mask is resolved without any irregularities. While in the center of the image the holes are separated very clearly from the background, on the outer edges the holes blur out. Due to the experimental

configuration the hole mask is not illuminated uniformly. The more the holes deviate from the center the steeper the incidence angle of the particles and the weaker the transmitted intensity. Therefore, the weakly imaged intensity on the outer edges is assumed not to be a property of the MCP but an artefact of the experiment. Illuminating the hole mask with particles in the far field approximation[1] will probably lead to a more uniform image.
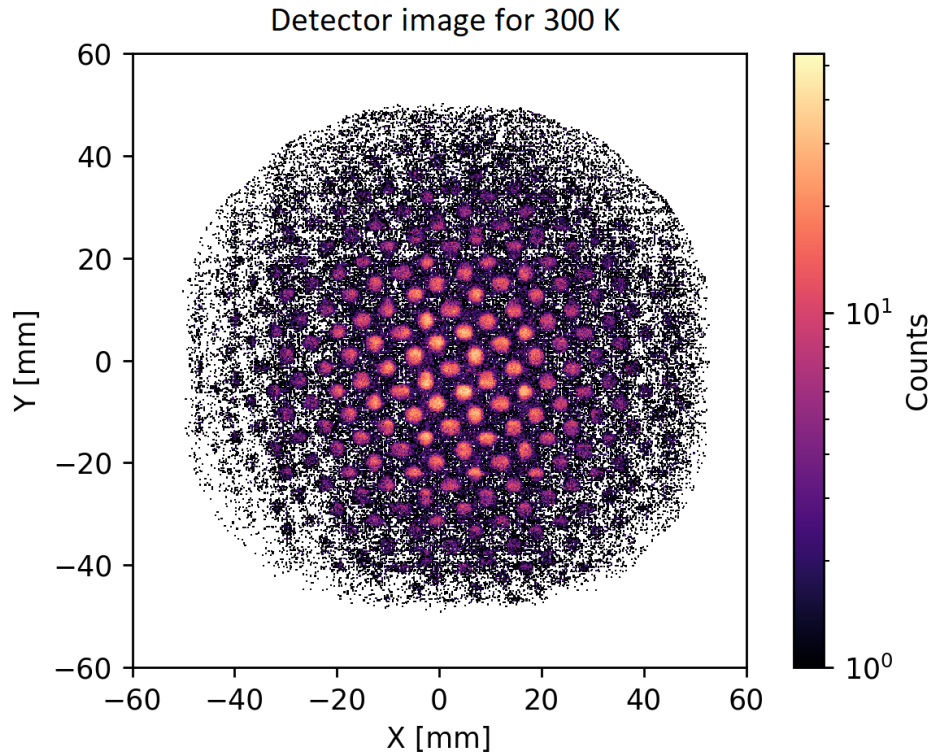

Figure 5.4.: Detector image of a hole mask between source and MCP for 300 K. The centered holes are resolved very clearly while the outer ones are displayed less exactly. The imaging capability of the detector shows no irregularities in resolving the linear pattern of the hole mask.

Compared to the image taken at 35 K (see Figure 5.5) the only considerable difference is the higher total intensity. Systematically more incident

---

[1]The far field approximation describes parallel wavefronts in wave optics or parallel rays in ray optics. Large distances to the source are needed to validate this approximation.

particles are displayed in the image, higher intensities across the hole structure as well as for the underground are measured. One possible explanation can be that the detector can be operated closer to saturation with less supply voltage when measuring at 35 K. Therefore, the detector is more efficiently producing detectable signals.
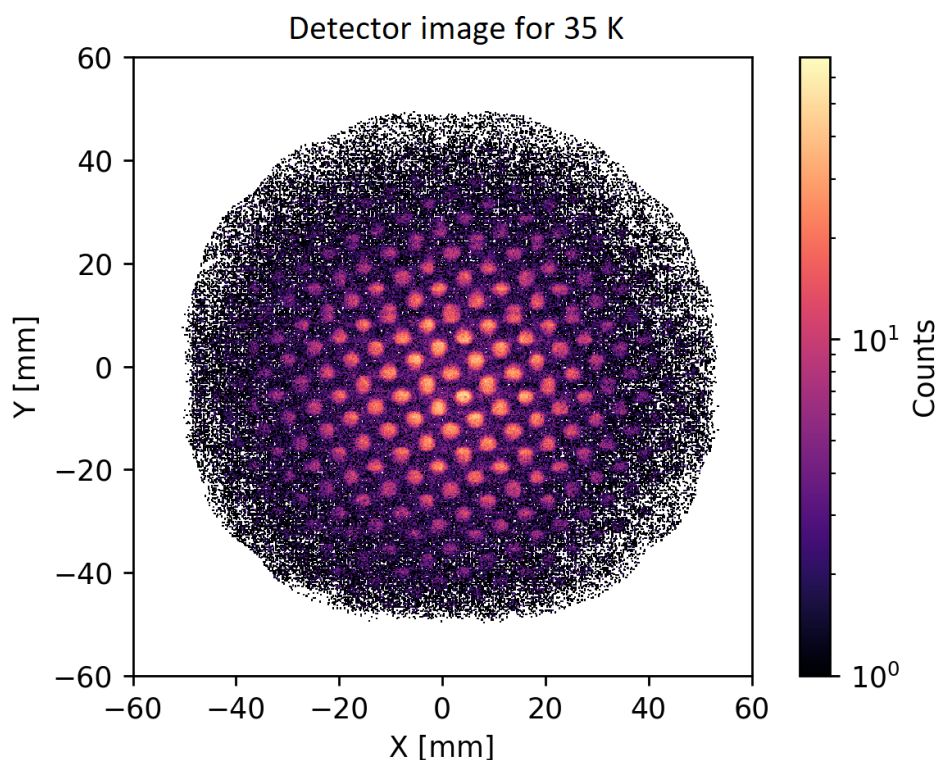

Figure 5.5.: Detector image of a hole mask between source and MCP for 35 K. Again the centered holes are resolved very clearly while the outer ones are displayed less exactly. The imaging capability of the detector shows no irregularities in resolving the linear pattern of the hole mask. Compared to the measurement at room temperature (Figure 5.4) it seems like there is more signal. The holes are depicted more clearly but also more noise in between the actual hole pattern can be observed.

6. Discussion and Outlook

The test setup for cryogenic tests of MCP detectors was built up and taken into operation. The setup reaches a temperature of $35\,\text{K}$, measured at the MCP front face electrode. $^{241}_{95}\text{Am}$ with a current activity of $34.2\,\text{kBq}$ was chosen as a particle source. The MCP detector contains a DDL for position resolved measurements and two doubly stacked (Chevron stacked) MCPs with an OAR of 0.6 and a quality diameter of $120\,\text{mm}$.

6.1. Results

To evaluate the saturation properties of the used channel plates the PHDs for different supply voltages were measured at room temperature and at $35\,\text{K}$. Comparing the results (Figure 5.2 at $300\,\text{K}$ and Figure 5.3 at $35\,\text{K}$) it can be assumed that the MCP is operated near the saturation limit for a supply voltage of $-3100\,\text{V}$. It can be qualitatively assumed that for $35\,\text{K}$ the saturation limit is reached at smaller supply voltages. The measurement rate remained unchanged for both temperatures. As a result it can be pointed out that the temperature change to $35\,\text{K}$ has no remarkable influence on the MCP performance as long as it is operated near saturation.

To testify the imaging properties of the MCP a linearity measurement was executed. A hole mask was mounted between the Am-source and the channel plate. Both, the image taken at room temperature (Figure 5.4) and the image taken at $35\,\text{K}$ (Figure 5.5) show the linear pattern of the hole mask without any irregularities. Since at lower temperatures the MCP is operated near saturation for smaller supply voltages and the voltage chosen for this measurement was $-2700\,\text{V}$, the image taken at $35\,\text{K}$ shows a higher total intensity. Also according to this measurement no significant differences between operating the MCP at room temperature or at $35\,\text{K}$

can be found.

6.2. Possible Future Improvements

During building up the experimental setup it turned out that the thermal conductivity of the used construction parts can not provide sufficient heat transport away from the MCP. The lowest possible temperature measured at the MCP front face is 35 K. To further lower this value one would have to replace all ceramic connection parts between the individual detector modules by sapphire crystals. Additionally, all wires connected to the detector or to temperature sensors have to be anchored by thermally connecting them to the outer shield. It could be thought of a sapphire clip mounted on the outer surface of the outer shield. Using this clip one ensures thermal connection and electrical isolation. Furthermore, an additional copper braid directly connecting the detector base plate to the second stage of the coldhead can be added. In a last step more super isolation can be used to protect the inner construction parts from external thermal radiation.

An electrical improvement would be an amplifier with adjustable gain. The used ORTEC FTA 820 provides a gain of $G = 200$ but it turned out that the MCP signal needs much less amplification than the anode signals. One main difficulty in configuring the built up setup is to find a proper supply voltage such that the MCP is operating near the saturation limit and such that the software does not lose too much signals due to its voltage limit of 1 V. With a far optimized setup one would be able to adjust every single channel of the ADC input independently. One could use a cascade of individually tuned attenuators or use a different amplifier with individual gain for every single channel.

Further, the following questions will have to be investigated before integrating the detector in the CSR.

i) What is the temperature where the PHD loses its Gaussian shape when a supply voltage of -3100 V is applied?

ii) Will the imaging capability of the detector decrease with further decreasing temperature?

iii) Can be found an electrical configuration where the MCP can be operated in the saturation region and the signals of all ADC channels can be displayed completely using the Cobold software?

And the main question remaining: Will it be possible to test the MCP at the specified CSR temperature of below $10\,\mathrm{K}$ when the improvements mentioned above are implemented?
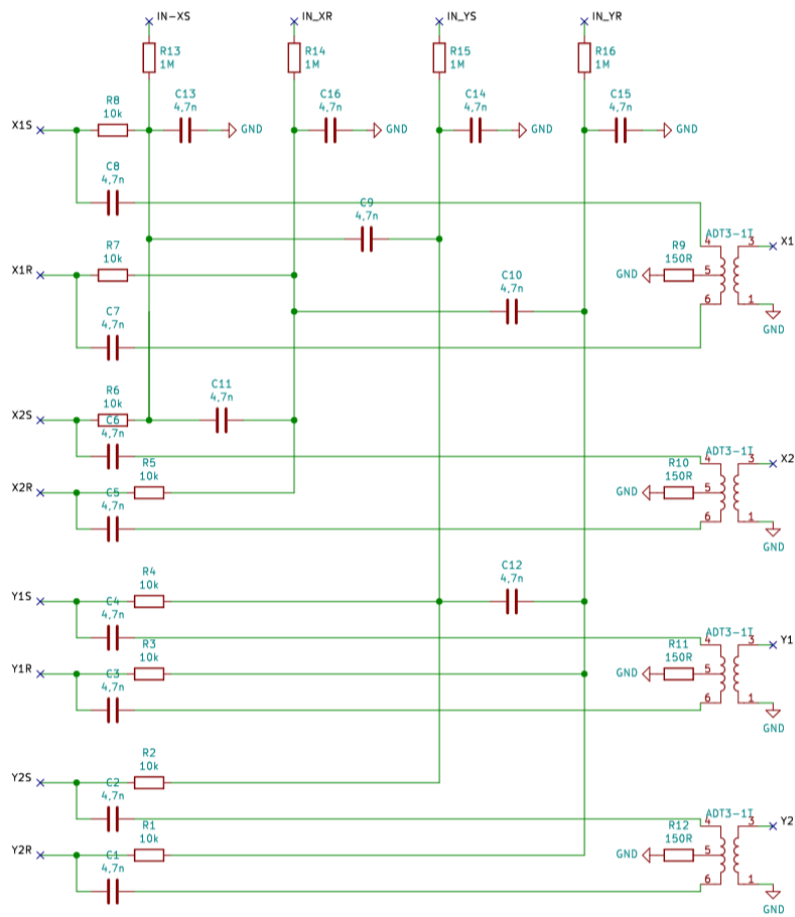
A. Appendix

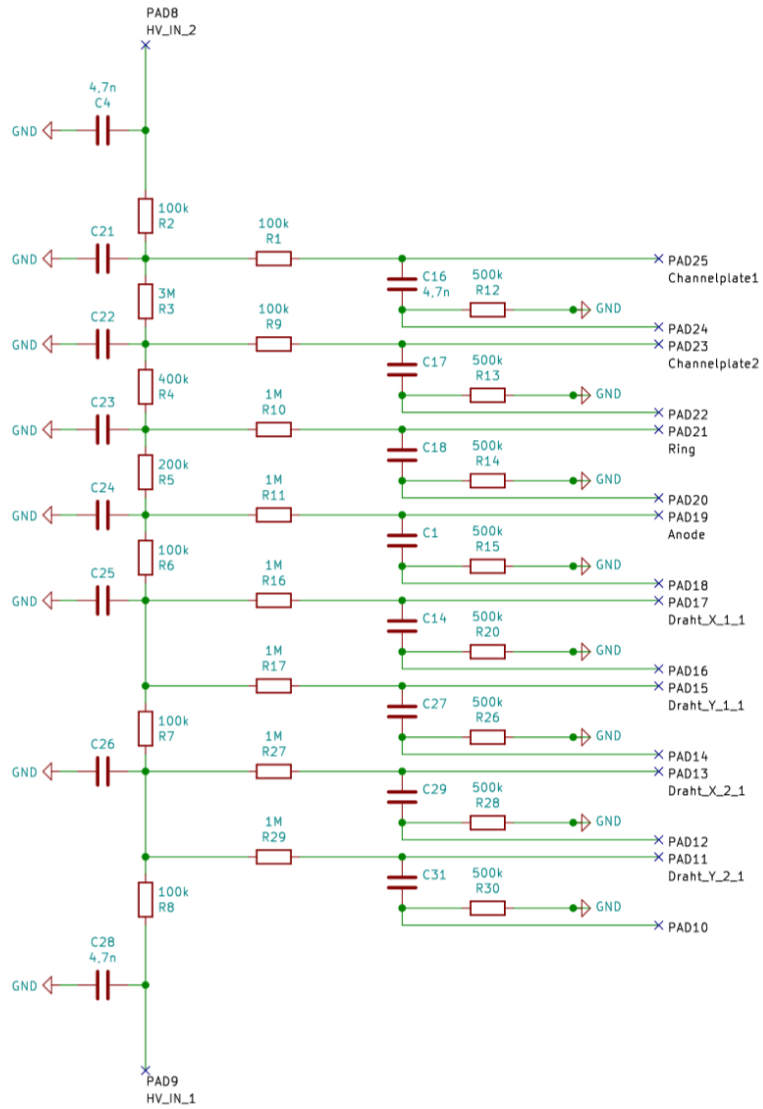**Figure A.1.:** Circuit diagram of VDB2.

Figure A.2.: Circuit diagram of VDB1.

Bibliography

[1] J. Boslough, "Stephen Hawking's universe," *New York: W. Morrow, c1985. 1st ed.* (1985) .

[2] A. Einstein, "Science and religion," 1940.

[3] K. Akiyama et al., "First m87 event horizon telescope results. iv. imaging the central supermassive black hole," *The Astrophysical Journal Letters* **875** no. 1, (2019) L4.

[4] A. Eddington, "Interstellar matter," *The Observatory* **60** (1937) 99–103.

[5] E. Herbst, *Interstellar Chemistry*, pp. 1–21. Springer Netherlands, 2001.

[6] D. Zajfman et al., "Physics with colder molecular ions: the Heidelberg Cryogenic Storage Ring CSR," *Journal of Physics: Conference Series* **4** no. 1, (2005) 296.

[7] R. Von Hahn et al., "The electrostatic cryogenic storage ring CSR-mechanical concept and realization," *Nuclear Instruments and Methods in Physics Research Section B* **269** no. 24, (2011) 2871–2874.

[8] R. Moshammer et al., "A 4π recoil-ion electron momentum analyzer: A high-resolution "microscope" for the investigation of the dynamics of atomic, molecular and nuclear reactions," *Nuclear Instruments and Methods in Physics Research Section B* **108** no. 4, (1996) 425–445.

[9] R. Moshammer et al., "The dynamics of target ionization by fast highly charged projectiles," *Nuclear Instruments and Methods in Physics Research Section B: Beam Interactions with Materials and Atoms* **107** no. 1-4, (1996) 62–66.

[10] J. Ullrich et al., "Recoil-ion and electron momentum spectroscopy: reaction-microscopes," *Reports on Progress in Physics* **66** no. 9, (2003) 1463.

[11] S. Hunklinger, *Festkörperphysik*. Oldenbourg Verlag, 2009. Fourth revised edition.

[12] R. Gross and A. Marx, *Festkörperphysik*. Walter de Gruyter GmbH & Co KG, 2018. Third revised edition.

[13] P. Roth and G. Fraser, "Microchannel plate resistance at cryogenic temperatures," *Nuclear Instruments and Methods* **439** no. 1, (2000) 134–137.

[14] D. Smith, "Channel multiplier operation in a reduced temperature environment," *Nuclear Instruments and Methods* **71** no. 2, (1969) 137–140.

[15] K. Fehre, "Absolute ion detection efficiencies of microchannel plates and funnel microchannel plates for multi-coincidence detection," *Review of Scientific Instruments* **89** no. 4, (2018) 045112.

[16] R. Wagner, "3D printed micro channel plate, method of making and using 3D printed micro channel plate," 2019. US Patent 10,403,464.

[17] A. Guest, "A computer model of channel multiplier plate performance," *Acta Electronica* **14** (1971) 79.

[18] M. Furman and M. Pivi, "Probabilistic model for the simulation of secondary electron emission," *Physical review special topics-accelerators and beams* **5** no. 12, (2002) 124404.

[19] Hamamatsu Photonics K.K., "MCP Assembly." `https://www.triumf.ca/sites/default/files/Hamamatsu%20MCP%20guide.pdf`. Online; accessed 07. April 2020.

[20] P. Soul, "Operational properties of channel-plate electron multipliers," *Nuclear Instruments and Methods* **97** no. 3, (1971) 555–565.

[21] K. Schmidt and C. Hendee, "Continuous channel electron multiplier operated in the pulse saturated mode," *IEEE Transactions on Nuclear Science* **13** no. 3, (1966) 100–111.

[22] C. Loty, "Saturation effects in channel electron multipliers (Current and charge saturation effects on channel electron multipliers in continuous and pulse operation)," *Acta Electronica* **14** (1971) 107–119.

[23] W. Colson et al., "High-gain imaging electron multiplier," *Review of scientific instruments* **44** no. 12, (1973) 1694–1696.

[24] J. Wiza et al., "Microchannel plate detectors," *Nucl. Instrum. Methods* **162** no. 1-3, (1979) 587–601.

[25] M. Galanti et al., "A high resolution, high sensitivity channel plate image intensifier for use in particle spectrographs," *Review of Scientific Instruments* **42** no. 12, (1971) 1818–1822.

[26] B. Tatry et al., "Characteristics of electron multipliers used as detectors for low energy protons," *Nuclear Instruments and Methods* **69** no. 2, (1969) 254–260.

[27] A. Tremsin, "Microchannel plate operation at high count rates: new results," *Nuclear Instruments and Methods in Physics Research Section A* **379** no. 1, (1996) 139–151.

[28] K. Kühnel et al., "Operating MCP detectors at cryogenic temperatures," *Proceedings of EPAC08, Genoa, Italy* (2008) 1179–1181.

[29] J. Schecker et al., "The performance of a microchannel plate at cryogenic temperatures and in high magnetic fields, and the detection efficiency for low energy positive hydrogen ions," *Nuclear Instruments and Methods in Physics Research Section A* **320** no. 3, (1992) 556–561.

[30] G. Eschard and B. Manley, "Principle and characteristics of channel electron multipliers," *Acta Electronica* **14** (1971) 19–39.

[31] Universität Bayreuth, "Cup-spring response curve." https://baymp.de/tfeder.html. Online; accessed 20. April 2020.

[32] A. Senftleben, *Kinematically complete study on electron impact ionisation of aligned hydrogen molecules.* PhD thesis, 2009.

[33] K. Schnorr, *XUV pump-probe experiments on electron rearrangement and interatomic coulombic decay in diatomic molecules.* PhD thesis, 2014.

[34] T. Pflüger, *Electron impact ionization studies of small rare gas clusters.* PhD thesis, 2012.

[35] C. Day, "Kryotechnik und Kryopumpen," *Springer* (2017) .

[36] R. Haefer, "Praktische Ausführung von Kryopumpen,".

[37] SHI Cryogenics Group, "Coldhead capacity map for model RDK-408D2." `http://www.shicryogenics.com/wp-content/uploads/2019/08/RDK-408D2_Capacity_Map.pdf`. Online; accessed 13. May 2020.

[38] M. Basunia, "Nuclear data sheets for A= 237," *Nuclear Data Sheets* **107** no. 8, (2006) 2323–2422.

Acknowledgements

Special thanks go to:

- **Claus Dieter Schröter** for a nice introduction to the topic and for always being patient with me. Without his help the setup would have never been built up and a lot of problems would still wait for a solution.

- **Robert Moshammer** for his pragmatic solutions. He always knows what to do. If the experiment survives the often radical methods, in the end it is always working better.

- **Patrick Froß** for the help with the data acquisition software and with the software tracking the temperatures, for proofreading this thesis and for providing mental support during tough times.

- **Achim Czasch** from RoentDek for correctly configuring the Cobold software and for always answering my numerous questions regarding the data acquisition.

- Tobias Heldt, Jakob Kaiser, Kevin Jahnke, Anne Harth for proofreading this thesis.

Once more, I would like to thank Kevin Jahnke and Jakob Kaiser for being my friends and exercise sheet partners during my whole university career. We overcame all the challenges university came up with and I am proud that we all three graduate with great results.

Erklärung:

Ich versichere, dass ich diese Arbeit selbstständig verfasst, und keine anderen als die angegebenen Quellen und Hilfsmittel benutzt habe.

Heidelberg, den 07. Oktober 2020 . . . .

Declaration:

I hereby certify that the thesis I am submitting is entirely my own original work except where otherwise indicated.

Heidelberg, October 7$^{\text{th}}$ 2020 . . . .